

# Self-Consistent Modeling of Nonlocal Inductively Coupled Plasmas

Oleg V. Polomarov, Constantine E. Theodosiou, Igor D. Kaganovich, Demetre J. Economou, and Badri N. Ramamurthi

**Abstract**—In low-pressure radio-frequency (RF) discharges, the electron-energy distribution function (EEDF) is typically non-Maxwellian for low plasma density. The nonlocal plasma conductivity, plasma density profiles, and EEDF are all nonlinear and nonlocally coupled. For accurate calculation of the discharge characteristics, the EEDF needs to be computed self-consistently. The method of fast self-consistent one-dimensional of planar inductively coupled discharges driven by a RF electromagnetic field is presented. The effects of a non-Maxwellian EEDF, plasma nonuniformity, and finite size, as well as the influence of the external magnetic field on the plasma properties are considered and discussed.

**Index Terms**—Anomalous heating, collisionless heating, plasma discharges, stochastic heating.

## I. INTRODUCTION

LOW-PRESSURE radio-frequency (RF) inductive-coupled plasma (ICP) are extensively used for plasma aided materials processing, semiconductor manufacturing, and lighting [1], [2]. For very low pressures, i.e., in the mtorr range, ICP discharges exhibit a strong nonlocal behavior and a number of peculiar physical effects typical of warm plasmas, such as anomalous skin penetration and a resonant wave-particle interaction [3]–[5]. Understanding of these effects can help design and optimization of the ICP sources, resulting in improvement of characteristics of plasma-based devices.

A gas discharge is a complex, nonlinear, multiparametric, self-organizing system, characterized by enormous disparity of temporal, spatial, and energy scales. Therefore, discharge simulations using “brute-force” numerical solutions of the governing equations (e.g., particle-in-cell/Monte Carlo collision) can be extremely time and labor consuming. For example, the simulation time step is limited typically by the electron plasma frequency, which is of the order of 0.1 ns, whereas the time needed to establish discharge steady-state is of the order of 10 000 ns [1]. One way to reduce the computational burden is

to implement fast kinetic modeling to eliminate fast time and small spatial scales by using appropriate space-time averaging procedures. The resulting averaged equations are usually much simpler, and can be effectively integrated using a desktop computer. This is important for analyzing engineering applications of discharge plasmas. Another benefit of fast kinetic modeling is gaining thorough insight in the discharge behavior, and this is not easily available through direct numerical modeling. The description of the one-dimensional (1-D), fast, self-consistent, kinetic modeling of low-pressure nonlocal ICP RF-discharges, is the main topic of this paper.

Note that, the formalism described here as applied to ICPs, can also be applied to other problems of wave-particle interaction in nonuniform plasmas, i.e., semiconductor physics, laser-plasma interactions, collective phenomena during propagation of intense beams, RF heating of plasmas in discharges and tokamaks, etc.

In the first part of this paper, the results of self-consistent numerical modeling of a nonuniform low-pressure plasma are presented, focusing on nonmagnetized ICP discharges. The pronounced influence of the electrostatic potential on plasma parameters at the bounce resonance condition is demonstrated [6]. This phenomenon is of importance in a wide range of problems related to penetration of electromagnetic waves into bounded low-pressure warm plasmas, and a similar formalism can be applied to a number of other cases [7].

The addition of the weak external magnetic field can substantially change the ICP discharge properties due to enhanced electron heating by electron cyclotron (ECR) and transmission resonances [8]. The influence of an external magnetic field on the plasma properties was extensively investigated in the 1960s–1970s in connection with plasmas in metals, and recently for gaseous ICP discharges [9]–[12]. However, most theoretical results were obtained for uniform plasmas and a prescribed electron energy distribution (EEDF) function (Fermian or Maxwellian). Self consistent kinetic calculation of the discharge plasma parameters, taking into account the plasma nonuniformity and possible nonequilibrium EEDF, is still a challenging task. A detailed description of fast, self-consistent modeling of nonuniform weakly-magnetized ICP discharges and analysis of the related ECR and transmission resonances are the topic of the second part of this paper.

The presented approach differs from the most previous analytical and semianalytical works on the low-pressure ICP as it allows a self-consistent treatment of the low-collisional, nonuniform plasmas with nonlocal conductivity operator. Having given atomic cross sections, discharge dimensions, and

Manuscript received October 4, 2005; revised January 23, 2005.

O. V. Polomarov was with the Department of Physics and Astronomy, University of Toledo, Toledo, OH 43606-3390 USA. He is now with the Institute for Fusion Studies, University of Texas at Austin, Austin, TX 78712 USA (e-mail: opoloma@physics.utexas.edu).

C. E. Theodosiou are with the Department of Physics and Astronomy, University of Toledo, Toledo, OH 43606-3390 USA (e-mail: ctheodo@utnet.utoledo.edu).

I. D. Kaganovich is with the Plasma Physics Laboratory, Princeton University, Princeton, NJ 08543 USA (e-mail: ikaganov@pppl.gov).

D. J. Economou and B. N. Ramamurthi are with the Plasma Processing Laboratory, Department of Chemical Engineering, University of Houston, Houston, TX 77204-4004 USA (e-mail: economou@uh.edu).

Digital Object Identifier 10.1109/TPS.2006.875733

applied power or the driving coil current, the presented model yields the consistent EEDF, the RF electric field, and plasma density profiles. Moreover 1) the possibility of modeling of the nonuniform plasmas with a non-Maxwellian EEDF differs the presented model from the other studies on nonlocal ICP such as [12]–[18] where a uniform plasma or a Maxwellian EEDF are used and 2) the possibility of the modeling of the nonlocal kinetic effects differs the model from the existing self-consistent treatments of the collisional discharges with local conductivity operators such as [19], [20].

## II. ENHANCED COLLISIONLESS HEATING IN NONUNIFORM NONMAGNETIZED PLASMA

An interesting effect that can lead to enhanced heating for bounded, low-pressure plasmas is a bounce resonance between the frequency  $\omega$  of the driving RF field and the frequency  $\Omega_b$  of the bounce motion of the plasma electrons confined into the potential well by an electrostatic ambipolar potential  $\phi(x)$  and the sheath electric fields near the plasma edges [13], [15], [21]–[23], [37]. Most earlier theoretical and numerical studies on this subject assumed for simplicity a uniform plasma density and the absence of an electrostatic potential. As a result, the electrons bounced inside a potential that is flat inside the plasma and infinite at the walls [13], [16]–[18]. Although these suppositions can result in a qualitative description of the plasma behavior under nonresonant conditions, the plasma parameters under resonant conditions can be greatly altered by accounting for the presence of the electrostatic potential, which always exists in real-life bounded plasmas.

It is a well-known result of the quasi-linear theory, that the electron heating of low-collisional, warm plasmas essentially depends on the resonant electrons, or electrons with velocities equal to the phase velocities of the plane waves constituting the RF field  $\omega = \mathbf{v} \cdot \mathbf{k}$  [22], [23], [37]. For bounded plasmas, the  $k$  spectrum is discrete, and the above condition transforms into the requirement that the RF field frequency must be equal to or be an integer ( $n$ ) multiple of the bounce electron frequency  $\omega = n\Omega_b$ . If the electron mean free path is much larger than the discharge gap  $L$ , the resonant electrons (with  $\Omega_b = \omega/n$ ) accumulate velocity changes in successive interactions with the RF electric field, which lead to a very effective electron heating [14], [21], [24]–[26]. The electron bounce frequency is very sensitive to the actual shape of the electrostatic potential, especially for low-energy electrons. Accounting for the electrostatic potential can bring the plasma electrons into a resonant region, even if they were not there in the absence of the potential. The increase of the number of the resonant electrons results into a drastic enhancement of the plasma heating.

### A. Basic Equation

Our model assumes a 1-D, slab geometry, ICP discharge of a plasma bounded on both sides by parallel walls with a gap length  $L$ , as it is shown in Fig. 1.

The surface currents, produced by an external RF source, flow in opposite directions. The induced RF electric field  $E_y$  is directed along the walls. The static electric field  $E_x = -d\phi/dx$ , directed towards the discharge walls, keeps electrons confined

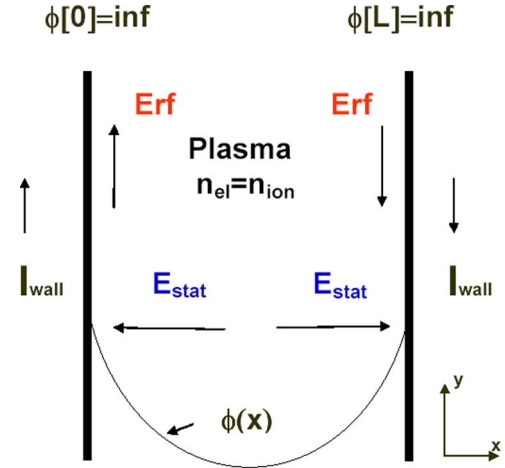


Fig. 1. 1-D model of bounded ICP. (Color version available online at <http://ieeexplore.ieee.org>.)

and the plasma quasi-neutral, i.e.,  $n_e(x) = n_i(x)$ . In the present treatment of plasmas with density  $n_e \sim 10^8 - 10^{12} \text{ cm}^{-3}$ , the sheath width is neglected, because it is of the order of a few hundreds of microns, which is small compared with the discharge dimension  $L$ . Furthermore, it is assumed that the plasma electrons experience specular reflection either at the discharge walls  $x_w = 0, L$  by the sheath electric field, if the electron energy  $\varepsilon_x = mv_x^2/2 - e\phi(x)$  is larger than  $-e\phi(x_w)$ , or at the turning points  $x_{\pm}(\varepsilon_x)$ , where  $-e\phi(x_{\pm}) = \varepsilon_x$ , by the static electric field in the plasma. The above 1-D scheme is a good approximation for a cylindrical ICP discharge, if the RF field penetration depth, or skin depth  $\delta$  into the plasma is less than the plasma cylinder radius  $R$  [27], [38]. Note, that the correspondence between 1-D geometry  $x, y$  used in this paper and the more practical cylindrical configuration is:  $x \rightarrow r, y \rightarrow \theta$ . In particular, for a cylinder  $E_{\text{stat}}$  is directed along  $\vec{e}_r$  and  $E_{\text{RF}}$  along  $\vec{e}_{\theta}$ .

A self-consistent study of the discharge properties involves calculation of the EEDF  $f_0(\varepsilon)$ , the RF electric field  $E_y(x)$ , and the ambipolar potential  $\phi(x)$ . The full description of the mathematical formalism is given in [6], [7], [28]. See also the second part of this paper where the upgraded version of the formalism with inclusion of external magnetic field is developed.

The EEDF  $f_0(\varepsilon)$  is obtained from the temporal-spatial averaged Boltzmann equation

$$-\frac{d}{d\varepsilon}(D_{\varepsilon} + \overline{D_{ee}}) \frac{df_0}{d\varepsilon} - \frac{d}{d\varepsilon}[\overline{V_{ee}} + \overline{V_{el}}] f_0 = St_{\text{inel}}. \quad (1)$$

Here, the upper bar denotes spatial averaging according to [28],  $St_{\text{inel}}$  is the inelastic collision integral and the coefficients  $V_{el}$ ,  $D_{ee}$  and  $V_{ee}$  stem from the elastic and electron–electron collision integrals, respectively, and are given in [29], [39].

The energy diffusion coefficient, responsible for electron heating, is given by

$$D_{\varepsilon}(\varepsilon) = \frac{\pi}{4} \sum_{n=-\infty}^{\infty} \int_0^{\varepsilon} d\varepsilon_x \times |\Delta v_y(\varepsilon_x)|^2 \frac{\varepsilon - \varepsilon_x}{\Omega_b(\varepsilon_x)} \times \frac{\nu}{[\Omega_b(\varepsilon_x)n - \omega]^2 + \nu^2} \quad (2)$$

where  $\nu$  is the collision frequency and  $\Omega_b(\varepsilon_x) = 2\pi/T_b(\varepsilon_x)$ , where  $T_b(\varepsilon_x) = 2 \int_{x_-}^{x_+} dx / \sqrt{2[\varepsilon_x + e\varphi(x)/m]}$  is the half of the bounce period of electron motion in the potential well, and  $\Delta v_y(\varepsilon_x) = e/m \int_0^{T_b(\varepsilon_x)} E_y[x(t)] e^{i\omega t} dt$  is the velocity kick acquired by an electron with energy  $\varepsilon_x$  during one bounce period [28].

Electric field is obtained from a single scalar equation

$$\frac{d^2 E_y}{dx^2} + \frac{\omega^2}{c^2} E_y = -\frac{4\pi i \omega}{c^2} [j(x) + I\delta(x) - I\delta(x-L)] \quad (3)$$

where  $I$  is the surface (coil) current and  $j(x)$  is the plasma electron current density calculated from the anisotropic part  $f_1$  of the EEDF, obtained from the linearized Boltzmann equation [28].

The electrostatic potential  $\phi(x)$  is obtained using the quasi-neutrality condition  $n_e(x) = n_i(x)$ , where  $n_e(x) = \int_{\varphi(x)}^{\infty} f_0(\varepsilon) \sqrt{\varepsilon - \varphi(x)} d\varepsilon$  is the electron density profile and  $n_i(x)$  is the ion density profile, obtained from a set of the fluid conservation equations for ion density and momentum [30], [40].

### B. Results and Discussion

The total power  $P$ , deposited into the plasma per unit square of a side surface, is related to the electron energy diffusion coefficient  $D_\varepsilon(\varepsilon)$  as [6], [28]

$$P = -\sqrt{2m} \int_0^\infty d\varepsilon D_\varepsilon(\varepsilon) \frac{df_0(\varepsilon)}{d\varepsilon}. \quad (4)$$

The dependence of plasma heating on resonant electrons is especially pronounced for  $\nu \ll \omega$ ,  $\Omega_b$  [7], because in this case the last factor on the right hand side of (2) tends to the Dirac delta function. As a result, the electron heating does not depend on the collision frequency and accounts explicitly for the bounce resonance

$$\Omega_b(\varepsilon_x) n = \omega. \quad (5)$$

However, if nonlinear effects are taken into account the collisionless heating may depend explicitly on the collision frequency [31]. Note that if  $L \rightarrow \infty$ , the summation in (2) can be replaced by integration over the corresponding wave vectors  $k$ , and the bounce resonance condition  $\Omega_b(\varepsilon_x) n = \omega$  transforms into the wave-particle resonance condition  $k_x v_x = \omega$  for a continuous wave spectrum.

The presence of ambipolar potential can greatly affect the electron heating due to the fact that the number of resonant electrons is generally larger for a nonuniform plasma than for a uniform plasma [7]. Eq. (2) shows that for  $\nu \ll \omega$  (when the effect of a bounce resonance is important) only resonant electrons, i.e., electrons in the energy range corresponding to  $|\Omega_b(\varepsilon_x) n - \omega| < \nu$ , or  $\Omega_b(\varepsilon_x) n \in [\omega - \nu, \omega + \nu]$  give essential contributions to the energy diffusion coefficient. As is evident from Fig. 2, which shows the dependence of the electron bounce

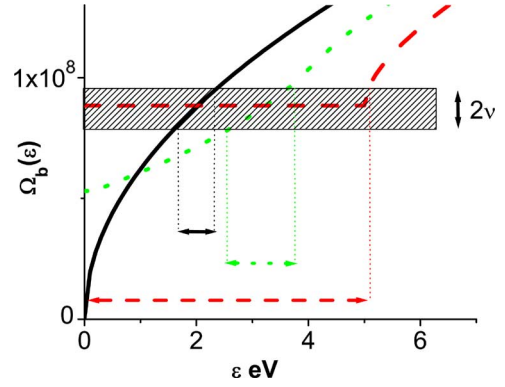


Fig. 2. Electron bounce frequency  $\Omega_b(\varepsilon_x)$ , as a function of the electron energy  $\varepsilon_x = mv_x^2/2 - e\phi(x)$  for different potential wells, consisting of the reflecting walls and different ambipolar potentials  $\phi(x)$ . Solid line corresponds to a uniform plasma with  $\phi(x) = 0$ , dashed line quadratic potential  $\phi(x) = 5 \times (2x/L - 1)^2$  eV and dotted line; the realistic potential obtained from the ion fluid model with  $T_e = 5$  eV. Discharge length is  $L = 3$  cm. Box of height  $2\nu$  shows the resonance region, corresponding to  $\omega = 8.52 \cdot 10^7$  s $^{-1}$ . Arrows show electron energies in the resonance region [6]. (Color version available online at <http://ieeexplore.ieee.org>.)

frequency  $\Omega_b(\varepsilon_x)$  on the electron energy  $\varepsilon_x$  for different potential wells, the number of resonant electrons increases if the ambipolar potential is taken into account. In the limit of a parabolic potential, the bounce frequency is the same for all electrons and *all electrons can be resonant simultaneously*. The realistic potential is close to parabolic in the discharge center and changes faster at the plasma periphery. As a result, the number of resonant electrons in nonuniform plasma is much larger than in uniform plasma, see Fig. 1.

To explicitly show the importance of accounting for ambipolar potential on the calculation of plasma heating, we performed numerical simulations of the plasma resistance for uniform and nonuniform plasmas (*with* and *without* ambipolar potential) for a given Maxwellian EEDF. Specifically, we obtained results for the plasma surface resistance, or the real part of the surface impedance  $Z = 4\pi/c \times E_0/B_0$ , as a function of the plasma length.  $E_0$  and  $B_0$  are the electric and magnetic field at the wall [5]. The plasma surface resistance is related to the power deposition as  $P = I^2 \text{Re}Z$ , where  $I$  is the effective amplitude of the driving current. From Fig. 3 it is evident that the presence of ambipolar potential significantly enhances plasma resistance under the bounce resonance condition ( $L \approx 2.6$  cm), comparing to the case of a uniform plasma. The most profound change in resistance is observed for a quadratic potential, because in this case all trapped electrons have the same bounce frequency, and, thus, all of them are resonant. The maximum of plasma surface resistance in Fig. 3 occurs due to the first bounce resonance  $n = 1$  in (5). At larger  $L$ , a smaller maximum exists due to the second resonance  $n = 2$  in (5). The obtained results explicitly show that neglecting the ambipolar potential, as is often done for simplicity, can lead to large discrepancies, especially for conditions close to the bounce resonance.

The bounce frequency increases with decreasing of the gap size for both uniform and nonuniform plasmas, but in the nonuniform plasma the bounce frequency for low energy electrons does not tend to zero, as shown in Fig. 2 and Fig. 6(c). As a result,  $\omega < \Omega_b$  can be satisfied for all electrons, which

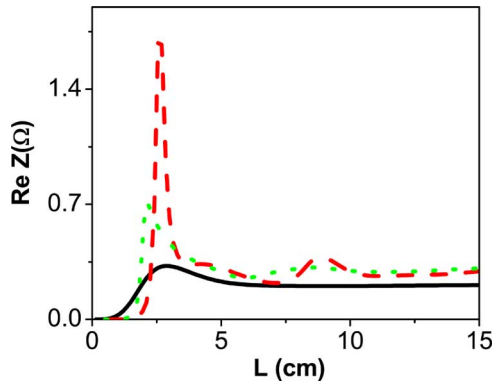


Fig. 3. Plasma resistance  $ReZ$  as a function of the discharge gap  $L$  for a uniform plasma (without any ambipolar potential: the solid line) and nonuniform plasma (quadratic potential: the dashed line, and the realistic potential obtained from the ion fluid model: the dotted line) with a given Maxwellian EEDF. Plasma parameters are: electron temperature  $T_e = 5$  eV, peak electron density at the discharge center  $n_e = 5 \times 10^{11}$  cm $^{-3}$ , RF field frequency  $\omega/2\pi = 13.56$  MHz, and the electron collision frequency  $\nu = 10^7$  s $^{-1}$  [6]. (Color version available online at <http://ieeexplore.ieee.org>.)

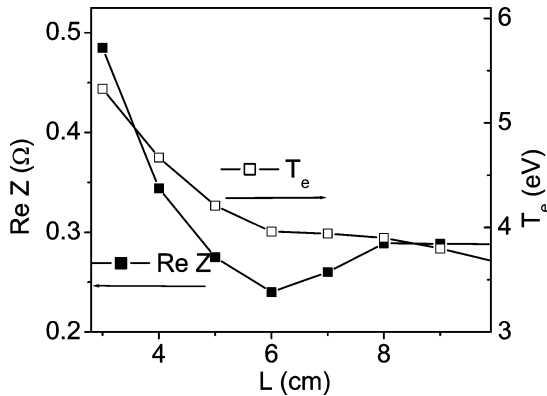


Fig. 4. Self-consistent simulations of the plasma surface resistance  $ReZ$  and the electron temperature  $T_e$  (defined as  $2/3$  of the average electron energy) at the discharge center as functions of the discharge gap. Discharge parameters are the coil current  $I = 5$  A/cm, the RF field frequency  $\omega/2\pi = 13.56$  MHz and Argon pressure  $P = 3$  mtorr [6].

leads to complete disappearance of the collisionless heating for small gaps in the nonuniform plasma [see Fig. 3 and Fig. 6(a)] in contrast to the limit of uniform plasma.

### C. Self-Consistent Simulations

The aforementioned phenomena has been observed in a fully self-consistent simulation of the EEDF, RF electric field, and ambipolar potential for a given coil current which have been performed for 13.56-MHz RF driving frequency.

Fig. 4 shows dependence of the plasma surface resistance on the discharge dimension. The simulations have been performed for discharge gaps in the range 3–10 cm (discharge can not be sustained for  $L < 3$  cm). The calculated plasma surface resistance has a sharp maximum for the resonant condition  $\omega = \Omega_b(\varepsilon_x)$ , which corresponds to the discharge gap 3 cm. Note that the plasma density is not a constant as in Fig. 2; it is approximately proportional to the plasma surface resistance, as more power ( $P = I^2 ReZ$ ) is deposited for larger  $ReZ$ .

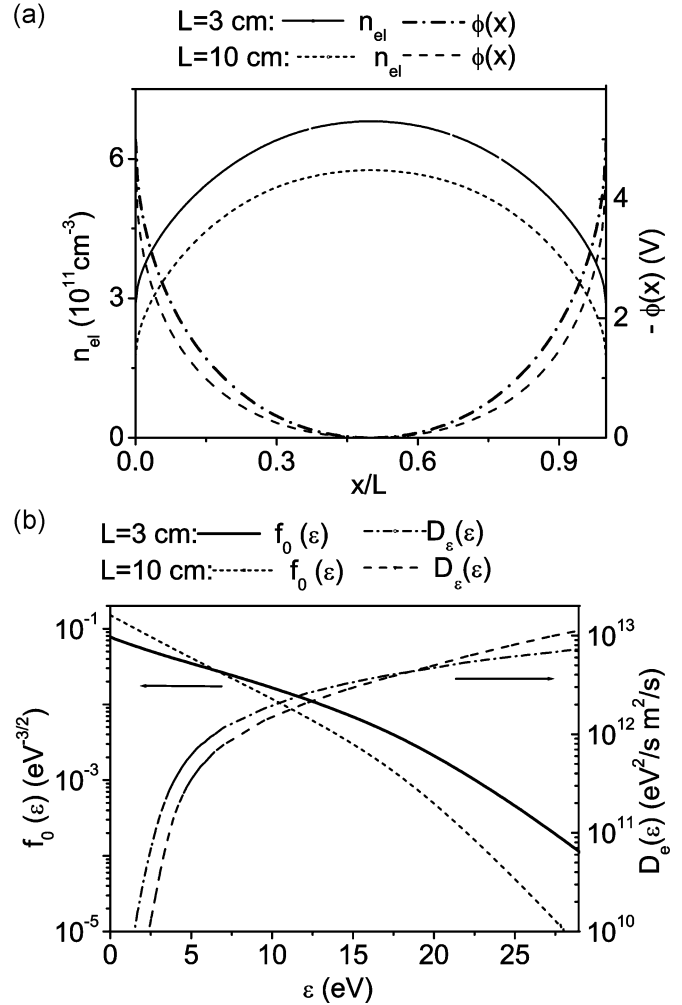


Fig. 5. Results of self-consistent simulations for the discharge gap  $L = 3$  cm corresponding to the bounce resonance, and  $L = 10$  cm for the same conditions as in Fig. 4. (a) Electron density and ambipolar potential profiles. (b) EEDF and the energy diffusion coefficient  $D_\varepsilon(\varepsilon)$  profiles.

The self-consistent electrostatic potential and ion–electron density profiles are plotted in Fig. 5(a) for two different discharge lengths: 3 cm, corresponding to the bounce resonance condition, and 10 cm, corresponding to the nonresonant width. These graphs show that the electron density at the center of the discharge is larger for 3-cm resonant gap than for 10-cm nonresonant gap. Note, if the power transfer efficiency, or the surface impedance were the same, then the total power transferred into the plasma were also the same and plasma densities were equal, due to energy balance. In our case, the surface impedance for 3-cm gap is considerably higher, what corresponds to the higher plasma density.

The electron energy distribution function and the diffusion coefficient in energy space are shown in Fig. 5(b). Fig. 5(b) shows that the energy diffusion coefficient is larger for 3-cm gap than for 10-cm gap for electron energy less than 15 eV. This results in more effective electron heating, leading to the larger plasma resistivity shown in Fig. 21.

The steady-state electron energy distribution function is governed by following processes: the collisionless electron heating

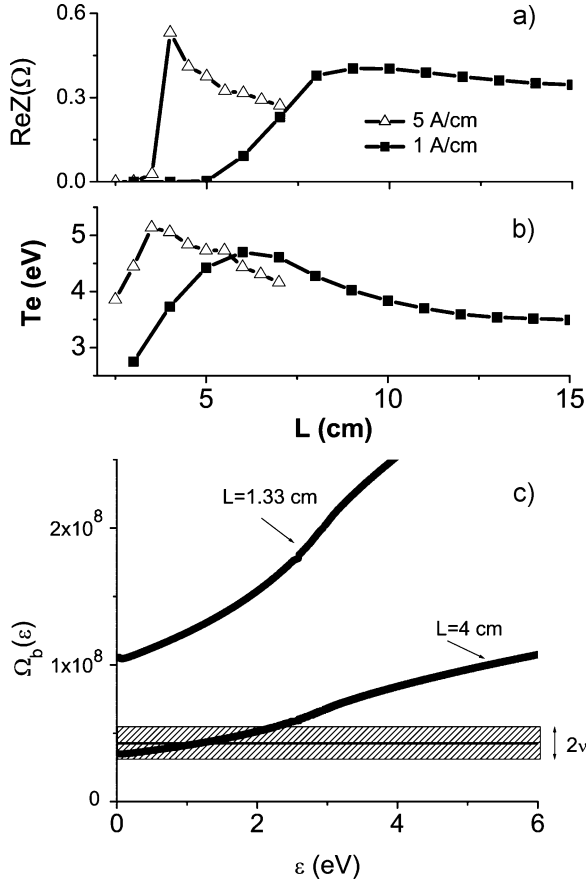


Fig. 6. Self-consistent simulations for coil currents  $I = 1$  A/cm and  $I = 5$  A/cm and the given discharge parameters:  $P = 3$  mtorr,  $\omega/2\pi = 6.78$  MHz. Shown are: (a) the plasma surface resistance; (b) the electron temperature in the discharge center versus the discharge gap; and (c) the electron bounce frequency [6].

in the RF electric field, inelastic collisions with neutrals, and redistribution of energy among plasma electrons due to electron–electron collisions. We see in Fig. 5(b) that the EEDF shape is similar to the two-temperature EEDF [4] with the temperature of the tail of the distribution being lower than the temperature of the main body of the EEDF, corresponding to the onset of inelastic collisional losses. For 3-cm gap, corresponding to the bounce resonance condition, the electron temperature of low-energy electrons (less than excitation potential 11.5 eV) is much higher than for 10-cm nonresonant gap. This effect is similar to the plateau formation on the EEDF governed by collisionless heating in the finite range of electron energies [22], [37]. Under conditions of Fig. 5, this plateau is not well pronounced, because it is smeared out by electron–electron collisions.

Additional simulations have been performed for the twice lower discharge frequency: 6.78 MHz. Fig. 6(a) shows the result of self-consistent simulation of the plasma surface resistance for two coil currents, 1 and 5 A/cm. For lower discharge frequencies, the first bounce resonance corresponds to larger  $L$ . Correspondingly, the maximum of plasma surface resistance shifts toward larger  $L$ , compare Fig. 4(a) and Fig. 3. However, the positions of the surface resistance maxima are different for different coil currents. This is due to the different plasma density and correspondingly skin depth in the two cases. The larger

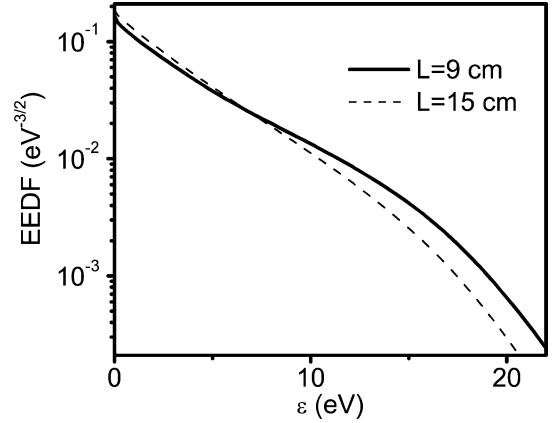


Fig. 7. EEDFs for the bounce resonance discharge gap length,  $L = 9$  cm, and for nonresonant discharge gap  $L = 15$  cm, for the surface current  $I = 1$  A/cm, and other conditions are the same as in Fig. 7.

coil current transfer a larger power into the plasma, which results in a higher plasma density. For example, for the condition of Fig. 6(a):  $n_e = 2 \times 10^{10}$  and  $n_e = 7 \times 10^{11}$  for 1 and 5 A/cm, respectively.  $n_e \sim P \sim I^2$  due to  $P \sim n_e v_{Bohm} \Delta \epsilon_i$  and  $P = -I^2 ReZ$ , where  $v_{Bohm}$  is the Bohm velocity and  $\Delta \epsilon_i$  is the ionization price [1]. The higher plasma density, in turn, leads to the smaller skin depth. Further, it follows from (4) and (2) that the electron heating is maximal if two conditions are met: the electron velocity kick  $\Delta v_y(\epsilon_x)$  is large for electron energies corresponding to the first bounce resonance  $\omega = \Omega_b(\epsilon_x)$ , and the fraction of the resonant electrons satisfying the bounce resonance condition is not small. The velocity kick amplitude  $\Delta v_y$  is maximal if transit time through the skin layer  $\delta/v_x$  is approximately equal to  $1/\omega$ , i.e.,  $\omega \approx v_x/\delta$  (transit resonance). Combining the transit resonance condition with the first bounce resonance condition  $\omega \approx v_x \pi/L$  estimated in uniform plasmas, yields  $L \approx \pi \delta$ . As it is shown in Fig. 1 and Fig. 6(c), the fraction of the resonant electrons is not small if  $\omega \delta \leq V_T$ , where  $V_T$  is the thermal velocity. Thus, the resulting rate of the electron heating depends on both transit and bounce resonances and is maximal when the both resonances are satisfied simultaneously, which occur at  $L \approx \pi \delta$ . Correspondingly, for larger discharge currents, the skin layer length is smaller and the position of the surface resistance maximum shifts into the region of smaller discharge gaps, as evident from Fig. 4(a). Similar results have been obtained in numerical simulations in [31] (see Fig. 2 of that paper).

Fig. 6(b) shows the electron temperature versus the discharge gap. Note, that our calculations show that the electron temperature grows with the increase of the discharge gap for small  $L$ . It differs from the predictions of the global model [1], [2] based on the Maxwellian EEDF and particle balance  $\nu_{ion}[T_e] = \nu_{loss}[T_e]$ , where  $\nu_{ion}$  is the ionization frequency and  $\nu_{loss}$  is the loss frequency. The difference is due to non-Maxwellian shape of the EEDF for the conditions of Fig. 6.

The electron energy distribution functions for 6.78 MHz are plotted in Fig. 7 for the surface current 1 A/m and for two different lengths, resonant 9 cm and nonresonant 15 cm. The phenomenon of plateau-formation on the EEDF is clearly seen for the bounce resonance condition for  $L = 9$  cm.

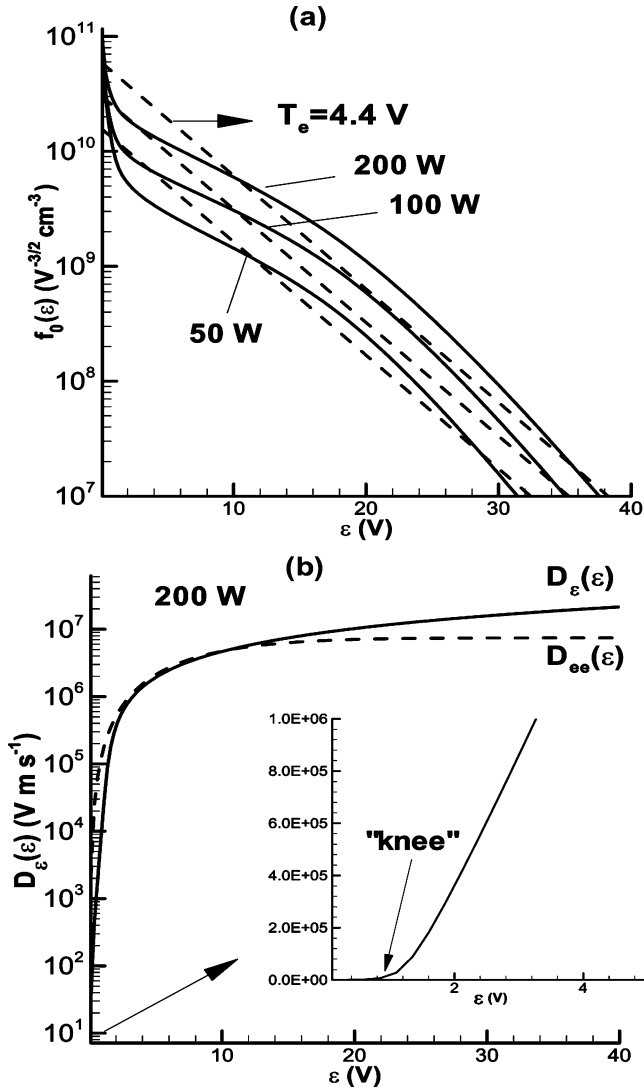


Fig. 8. (a) Self-consistently predicted non-Maxwellian (solid lines) and Maxwellian (dashed lines) electron energy distribution function (EEDF) as a function of total energy for 1 mtorr. (b) Energy diffusion coefficient [2]  $D_\epsilon(\epsilon)$  (solid line) and energy diffusivity (see text) related to e-e collisions (dashed line) as a function of total energy for 1 mtorr. Inset shows an expanded scale for  $D_\epsilon(\epsilon)$  [30], [40].

#### D. Comparison of Plasma Parameters With Maxwellian and Non-Maxwellian EEDFs

Here, the plasma properties, simulated using non-equilibrium (non-Maxwellian) and equilibrium (Maxwellian) EEDFs, are presented. It is shown, that the calculated plasma parameters can be drastically different for different EEDFs used. It suggests that the realistic plasma simulations must necessarily include the self-consistent treatment of nonequilibrium EEDF.

Results in Figs. 8–11 are for a pressure of 1 mtorr, discharge frequency of 13.56 MHz and discharge length 5 cm [30], [40]. Under these conditions the electron collision frequency is small compared to the applied field frequency. In each case, profiles calculated using the non-Maxwellian EEDF (solid lines) are compared with profiles (dashed lines) obtained using the Maxwellian EEDF approximation (see [30] and [40]) under the same discharge conditions and for the same (integrated) total power. Values of power correspond to a plate cross sectional area of 64 cm.

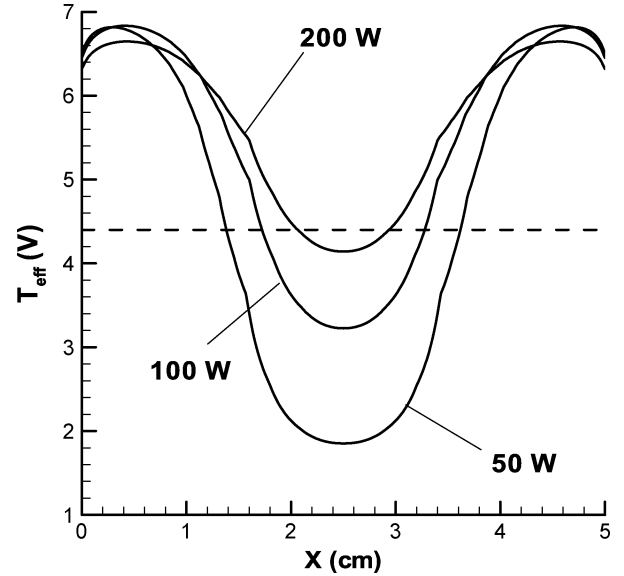


Fig. 9. Effective temperature profiles for a non-Maxwellian EEDF (solid lines) and a Maxwellian EEDF (dashed lines) for 1 mtorr [30], [40].

Fig. 8(a) shows the EEDF as a function of total energy for non-Maxwellian (solid lines) and Maxwellian (dashed lines) cases. The non-Maxwellian EEDF has a higher fraction of electrons just beyond the ionization threshold, predicting a higher ionization rate. For a pressure of 1 mtorr, the electron collision frequency  $3 \times 10^6 \text{ s}^{-1}$  and  $\nu/\Omega_b \sim 0.1$ . The energy diffusion coefficient  $D_\epsilon(\epsilon)$  of (2), exhibits a “knee” at 1 V [Fig. 4(b)], indicating that the “temperature” of electrons with energies less than 1 V is lower than that of electrons with energies greater than 1 V. The “knee” in Fig. 4(b) arises due to a phenomenon called “bounce heating” or “resonant heating.” For  $\nu/\Omega_b \sim 0.1$ , the energy diffusion coefficient in (13) can be approximated as

$$D_\epsilon(\epsilon) \sim \sum_{n=-\infty}^{\infty} \int_0^\epsilon d\epsilon_x \times |\Delta v_y(\epsilon_x)|^2 \frac{\epsilon - \epsilon_x}{\Omega_b(\epsilon_x)} \delta[\Omega_b(\epsilon_x)n - \omega] \quad (6)$$

where,  $\delta[\Omega_b(\epsilon_x)n - \omega]$  represents the Dirac-delta function. It can be seen from (6) that for energy  $\epsilon < \epsilon_1$  (where  $\epsilon_1$  is obtained from  $\Omega_b(\epsilon_1) = \omega$ ,  $D_\epsilon(\epsilon) \sim 0$ ). For  $\epsilon_1 < \epsilon < \epsilon_2$  (where  $\Omega_b(\epsilon_2) = \omega/2$ ),  $D_\epsilon(\epsilon) \sim (\epsilon - \epsilon_1)$ , i.e., the energy diffusion coefficient increases linearly with total energy. This behavior leads to the “knee” observed in Fig. 8(b), and implies that electrons with energy  $\epsilon_1$  (in this case is 1 V) are in resonance with the field and are thus heated more efficiently. Higher order resonant modes ( $n = 2, 3, 4, \dots$ ) contribute less as the Fourier coefficients of the electric field decrease as  $n$  increases. The dashed line in Fig. 8(b) shows the dependence on total energy of the e-e collision diffusivity term [given by  $D_{ee}(\epsilon)$  in (1)]. =m

Fig. 9 shows the screening temperature profiles given by (28) for the Maxwellian and non-Maxwellian EEDFs. For the Maxwellian case, the electron temperature is independent of power while for the non-Maxwellian case, significant differences are observed with power. The large difference between the temperatures at the edge and the center may be explained by examining Fig. 8(a) (solid lines). The EEDF shows that electrons with total energies less than 1 V are not effectively

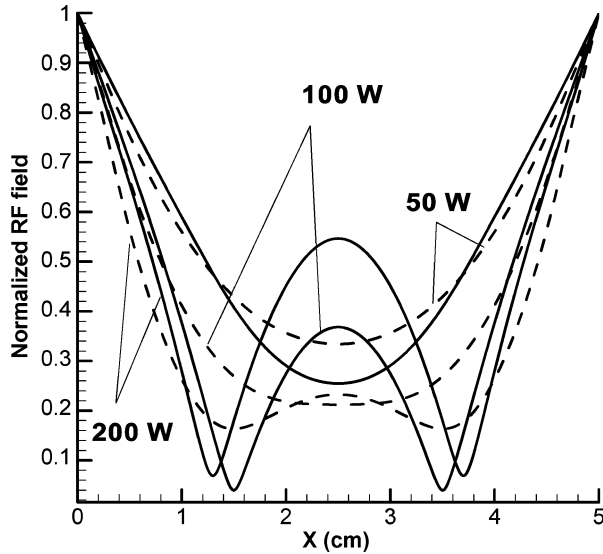


Fig. 10. Normalized amplitude of the RF field for 1 mtorr. Results using non-Maxwellian EEDF (solid lines) are compared with results using Maxwellian EEDF (dashed lines), under otherwise identical conditions [30], [40].

heated. Electrons with such low energies are essentially trapped near the discharge center (where the heating field is weak) as they cannot overcome the electrostatic potential barrier. Hence, the effective temperature at the center is low. In contrast, electrons with relatively high energies can overcome the potential barrier and reach the edge where the field is strong, and the effective temperature at the periphery (and larger total energies) is high. Note that even for the highest plasma density in Fig. 4, the electron–electron mean free path is about 10 m for 1 eV electrons, much higher than the interelectrode gap. Therefore, the electron–electron and collisionless energy diffusion coefficients are comparable at very low energy, 1 eV, see Fig. 4. As a result, low energy electrons form a Maxwellian distribution with very low temperature, 1 eV. Note that the part of the EEDF corresponding to such cold electrons is difficult to measure experimentally. The effective temperature profile becomes less nonuniform as power is increased, because of higher electron density resulting in more “thermalization” of the distribution by e–e collisions. The discrepancy between the Maxwellian temperature and the effective temperature near the edge induces a difference in the effective electron mean free path, which leads to considerably different field and current density

Fig. 10 shows the profiles of the normalized amplitude of the RF field. The field profile is monotonic for low power. However, for high power, the behavior becomes progressively non-monotonic due to increasing nonlocality. Specifically, the skin depth decreases with power, and the more energetic electrons can escape from the skin layer during a RF cycle, resulting in nonlocal behavior and nonmonotonic RF field profiles. The effect of nonlocality is more pronounced for the non-Maxwellian EEDF, especially for higher powers for which the RF field at the discharge center is more than 50% of the value at the edge. This is a direct consequence of the higher effective temperature predicted by the non-Maxwellian EEDF near the edge compared to the Maxwellian case. Warmer electrons can reach further in

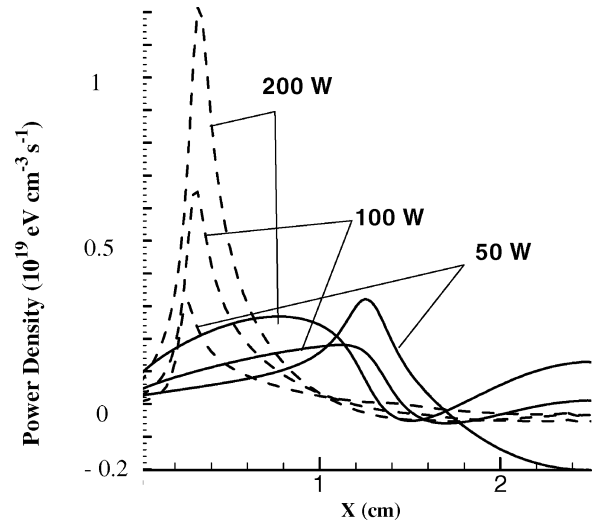


Fig. 11. Power density profiles for 1 mtorr. Results using non-Maxwellian EEDF (solid lines) are compared with results using Maxwellian EEDF (dashed lines), under otherwise identical conditions [30], [40].

the discharge core. The corresponding power deposition profiles are shown in Fig. 11. The peak of power deposition in the Maxwellian case is seen to occur closer to the boundary, when compared to that of the non-Maxwellian case. This is because of the higher effective temperature of electrons in the skin layer for the non-Maxwellian case, which causes them to travel a greater distance during an RF cycle. Both cases exhibit negative power deposition near the discharge center. This can be explained by the phase difference between the current and the RF field; electrons can pick up energy from the field within the skin layer and lose energy back to the field outside the skin layer. Negative power deposition has been observed experimentally for low-pressure inductively coupled discharges [16].

The corresponding positive ion density profiles are shown in Fig. 12. The positive ion density is determined by two factors: 1) the effective electron temperature at the boundary, which controls the loss rate of ions to the wall and 2) the rate of ionization (ground-state and metastable) [30], [40]. The latter depends on the tail of the EEDF beyond the ionization threshold of 15.76 V (ground state ionization dominates under these conditions). The ionization rate was found to be marginally higher for the non-Maxwellian EEDF. However, the effective temperature at the wall for the non-Maxwellian case (6.5 V) is larger than the Maxwellian temperature of 4.4 V (Fig. 9), leading to larger losses for the non-Maxwellian EEDF. This results in lower density for the non-Maxwellian case. The differences in the peak densities are 32.4%, 38.8%, and 44.4 %, respectively, for 50, 100, and 200 W.

### III. SELF-CONSISTENT TREATMENT OF LOW-MAGNETIZED ICP PLASMA

Application of a weak constant external magnetic field to low-pressure bounded plasma can drastically change its electrodynamics, due to possibility of the electron–cyclotron resonance (ECR), when  $\omega = \Omega_c$ , and the appearance of the new propagating wave modes for  $\omega > \Omega_c$ . These can result in more effective power transfer into plasma and possible transmission

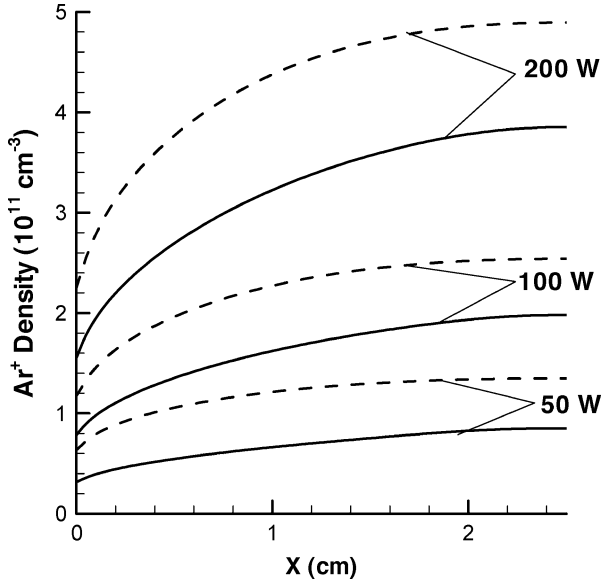


Fig. 12. Variation of ion density for 1 mtorr. Results using non-Maxwellian EEDF (solid lines) are compared with results using Maxwellian EEDF (dashed lines), under otherwise identical conditions [30], [40].

resonances (when the induced plasma field is close to one of the Fourier harmonics) [8]–[12]. Here,  $\omega$  is the RF driving frequency and  $\Omega_c = eB/m$  is the electron cyclotron frequency ( $e$  is the electron charge,  $m$  is the electron mass, and  $B$  is the magnetic field induction). A description of a fast self-consistent treatment of a weakly-magnetized plasma and investigations of plasma parameters under resonance conditions are the main topics of this section.

#### A. Basic Equations

The system under consideration assumes a 1-D slab geometry ICP discharge of a plasma bounded on both sides by two parallel walls with a gap length  $L$ . For the case of the cylindrical like geometry (two current sheaths), both walls carry prescribed currents, produced by an external RF source, flowing in opposite directions, and for the case of one grounded electrode: one of the walls is grounded, correspondingly.

The external magnetic field  $B$  is applied perpendicularly to the discharge plates, as it is shown in Fig. 13. The induced solenoidal RF electric field  $E_y$  and  $E_z$  is directed along the walls and the static ambipolar electric field  $E_{sc}$  of the ambipolar potential  $\phi(x)$  is directed towards the discharge walls, keeping the plasma quasi-neutral,  $n_e(x) = n_i(x)$ . In the present treatment of high density discharge plasmas ( $n_e \sim 10^8/10^{12} \text{ cm}^{-3}$ ), the sheath width is neglected, because it is of the order of a few hundreds of microns, much less than the discharge dimension  $L$ . Furthermore, it is assumed that the plasma electrons experience specular reflection: 1) from the discharge walls when they have total energy  $\varepsilon = mv^2/2 - e\phi(x)$  larger than the potential at the walls  $\varphi_w$ , and 2) from the geometrical location of the turning points  $x_-(\varepsilon)$ ,  $x_+(\varepsilon)$  when the the plasma electrons are confined into the potential well  $\phi(x)$ . The 1-D slab geometry system of two surface currents flowing in opposite directions provides a good description of a solenoidal discharge with diameter  $D = L$  [27], [38] and also describes approximately a “pancake” geometry with one coil at  $x = 0$  and a grounded electrode at  $x = L/2$

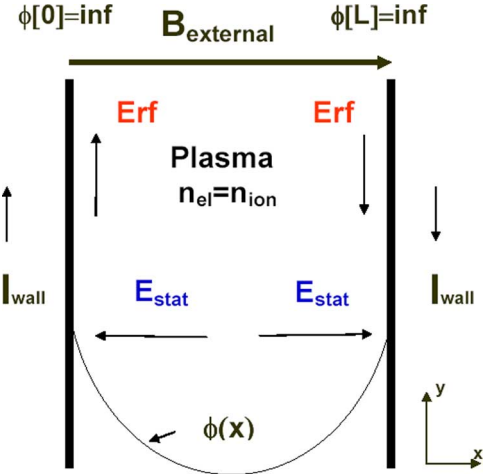


Fig. 13. 1-D model of magnetized ICP. The external magnetic field goes perpendicularly to walls. RF electric field has also a component along  $z$  axis. (Color version available online at <http://ieeexplore.ieee.org>.)

(corresponding to the boundary condition  $E_y = 0$  at  $x = L/2$ ) [28]. In this paper, we preferentially use the 1-D slab geometry of two surface currents (if it is not stated otherwise), because the analytical solution in this case is much simpler and easier to analyze, while results are similar to the just mentioned configurations for typical plasma parameters (see Appendix A for details). As for nonmagnetized plasmas, the correspondence between 1-D geometry  $x$ ,  $y$  of Fig. 13 and the realistic cylindrical configuration is:  $x \rightarrow r$ ,  $y \rightarrow \theta$  ( $E_{stat} \rightarrow E_r$  and  $E_{RF} \rightarrow E_\theta$ ).

In order to describe the discharge self-consistently, one needs to determine the induced RF electric field profiles  $E_{y,z}(x)$ , EEDF  $f_0(\varepsilon)$ , and the plasma density profile, or corresponding ambipolar potential  $\phi(x)$ . The detailed description of all the needed formalism for nonmagnetized discharges is given in [28]. A short account of the formalism, that is applicable to the magnetized plasmas (which is the straightforward generalization of the formalism for the nonmagnetized case) is given below.

#### B. Calculation of the EEDF

For the case of low-pressure, low-temperature discharges, when an energy relaxation length is large comparing to the plasma width and an energy relaxation time is large comparing to the RF period, the electron velocity distribution function (EVDF) can be represented as a sum of a main isotropic part  $f_0(\varepsilon)$  (EEDF), that is a function of only the total energy  $\varepsilon$ , and of a small alternating anisotropic part  $f_1(x, \mathbf{v}, t)$ ,  $f = f_0(\varepsilon) + f_1(x, \mathbf{v}, t)$  [29], [34], [36], [39]. The Boltzmann equation for the electron velocity distribution function, after applying the formalism of quasi-linear approach can be split into two equations (see Appendix B), one for the EEDF  $f_0$ , and the other for  $f_1(x, \mathbf{v}, t)$  (used for calculation of the energy diffusion coefficient and the nonlocal conductivity operator). Note, that the EVDF can be represented as two-term expansion  $f_0(\varepsilon) + f_1(x, \mathbf{v}, t)$  if the RF-quiver velocity is much less than the thermal velocity  $V_{RF}/V_T \ll 1$ , or  $(eE_{RF}/\sqrt{m^2(\omega^2 + \nu^2)})/\sqrt{kT/m} \ll 1$  [28]. For  $\omega \gg \nu$ , it yields  $(e^2 E^2/m\omega^2)/kT \ll 1$ . As a consequence, our approach is valid only if the ponderomotive potential can be neglected

(see, also, Appendix B). The description of effects of the RF magnetic field and ponderomotive force on the low-frequency ICP can be found in [3].

The final equation for the electron energy distribution function  $f_0$  is

$$-\frac{d}{d\varepsilon}(D_\varepsilon + \overline{D_{ee}}) \frac{df_0}{d\varepsilon} - \frac{d}{d\varepsilon}[\overline{V_{ee}} + \overline{V_{el}}] f_0 = \sum_k \left[ \nu_k^*(w + \varepsilon_k^*) \frac{\sqrt{(w + \varepsilon_k^*)}}{\sqrt{w}} f_0(\varepsilon + \varepsilon_k^*) - \overline{\nu_k^*} f_0 \right]. \quad (7)$$

Here, the bar denotes averaging according to (82), and  $\nu_k^*$  is the inelastic collision frequency. The coefficients  $V_{el}$ ,  $D_{ee}$ ,  $V_{ee}$  stem from the elastic and electron–electron collision integrals, respectively, and are given by [29], [35], [39]

$$V_{el} = \frac{2m}{M} w \nu \quad (8)$$

$$V_{ee} = \frac{2w\nu_{ee}}{n} \left( \int_0^w dw \sqrt{w} f \right) \quad (9)$$

$$D_{ee} = \frac{4}{3} \frac{w\nu_{ee}}{n} \left( \int_0^w dw w^{3/2} f + w^{3/2} \int_w^\infty dw f \right) \quad (10)$$

$$\nu_{ee} = \frac{4\pi\Lambda_{ee}n}{m^2\nu^3} \quad (11)$$

where  $w = mv^2/2$  is the electron kinetic energy,  $\nu_{ee}$  is the Coulomb collision frequency, and  $\Lambda_{ee}$  is the Coulomb logarithm.

The energy diffusion coefficient responsible for the electron heating is given by

$$D_\varepsilon(\varepsilon) = \frac{\pi e^2}{8m^2} \sum_{n=-\infty}^{\infty} \int_0^\varepsilon d\varepsilon_x |E_n^+(\varepsilon_x)|^2 \frac{\varepsilon - \varepsilon_x}{\Omega_b(\varepsilon_x)} \times \frac{\nu}{[\Omega_b(\varepsilon_x)n - (\omega + \Omega_c)]^2 + \nu^2} + \frac{\pi e^2}{8m^2} \sum_{n=-\infty}^{\infty} \int_0^\varepsilon d\varepsilon_x |E_n^-(\varepsilon_x)|^2 \frac{\varepsilon - \varepsilon_x}{\Omega_b(\varepsilon_x)} \times \frac{\nu}{[\Omega_b(\varepsilon_x)n - (\omega - \Omega_c)]^2 + \nu^2}. \quad (12)$$

Note that the expression for  $D_\varepsilon(\varepsilon)$  explicitly accounts for the Doppler shifted electron–cyclotron resonance  $\Omega_c + \Omega_b(\varepsilon_x)n = \omega$ . The dependence of electron plasma heating on resonant electrons especially pronounced for the  $\nu \ll \omega$ , as in this case

$$\frac{\nu}{[\Omega_b(\varepsilon_x)n - (\omega - \Omega_c)]^2 + \nu^2} \rightarrow \pi \delta(\Omega_b n - \omega + \Omega_c) \quad (13)$$

where  $\delta()$  is a Dirac delta function. It is worth to note that if  $L \rightarrow \infty$ , the summation in (13) goes into integration over corresponding wave vectors  $k_n$ , and the above mentioned resonance

condition transforms into the well-known ECR resonance condition for continuous wave spectrum  $\Omega_c + kv = \omega$ .

### C. Calculation of the RF Electric Field

The transverse RF electric fields  $E^\pm$  is obtained from a single scalar equation

$$\frac{d^2 E^\pm}{dx^2} + \frac{\omega^2}{c^2} E^\pm = -\frac{4\pi i \omega}{c^2} [j(x)^\pm + I \delta(x) - I \delta(x-L) \delta_{\text{anti}}], \quad (14)$$

where  $I$  is the wall current ( $\delta_{\text{anti}} = 0$  for one grounded electrode, and  $\delta_{\text{anti}} = 1$  for two current sheaths) and  $j(x)^\pm$  are the induced electron plasma current densities that can be calculated knowing the anisotropic part  $f_{1s}$  of the EVDF

$$j^\pm(x) = -\frac{em^{3/2}}{4\pi\sqrt{2}} \int f_{1s}(v_y \pm iv_z) d^3\mathbf{v} = -\frac{em^{3/2}}{4\pi\sqrt{2}} \int f_{1s} v_\perp e^{\pm i\phi} d^3\mathbf{v} \quad (15)$$

which can be rewritten after some transformations as

$$j^\pm(x) = \frac{e^2}{2m} \sum_{n=-\infty}^{\infty} \int_{\varphi(x)}^{\infty} \frac{\Gamma(\varepsilon)}{\sqrt{\varepsilon - \varphi(x)}} \frac{E_n^\pm \cos[n\theta(x)]}{in\Omega_b - i(\omega \pm \Omega_c) + \nu} d\varepsilon \quad (16)$$

where

$$\Gamma(\varepsilon) = \int_\varepsilon^\infty f_0(\varepsilon) d\varepsilon. \quad (17)$$

After mathematical continuing of the RF field outside of the slab as  $E^\pm(x) = E^\pm(-x)$ , and using the Fourier series

$$E^\pm(x) = \sum_{s=0}^{\infty} \Xi_s^\pm \cos(k_s x) \quad (18)$$

and

$$j^\pm(x) = \sum_{s=0}^{\infty} J_s^\pm \cos(k_s x) \quad (19)$$

the (14) yields

$$\left(-k_s^2 + \frac{\omega^2}{c^2}\right) \Xi_s^\pm = -\frac{4\pi i \omega}{c^2} \left[ j_s^\pm + \frac{(I + \delta_{\text{anti}})}{L} \right] \quad (20)$$

$$j_s^\pm = \frac{e^2}{m} \frac{1}{(2s+1)\Omega_{bT}} \times \sum_{l=0}^{\infty} \Xi_l^\pm Z_{s,l}^{\text{gen}} \left( \frac{(\omega \pm \Omega_c) + i\nu}{(2s+1)\Omega_{bT}} \right) \quad (21)$$

where  $s$  is an integer,  $k_s = (2s+1)\pi/L$  for cylindrical geometry and  $k_s = (2s+1)\pi/(2L)$  for one grounded electrode,

$\Omega_{bT} = v_T \pi / L$ , and we introduced the generalized plasma dielectric function

$$Z_{s,l}^{\text{gen}}(\xi) \equiv \sqrt{\frac{2}{m}} \frac{(2s+1)\pi\Omega_{bT}}{L} \times \sum_{n=-\infty}^{\infty} \int_0^{\infty} \frac{\Gamma(\varepsilon)}{n\Omega_b(\varepsilon) - (2s+1)\Omega_{bT}\xi} \frac{G_{s,n}(\varepsilon)G_{l,n}(\varepsilon)}{\Omega_b(\varepsilon)} d\varepsilon \quad (22)$$

where the coefficients  $G_{l,n}(\varepsilon)$  are the temporal Fourier transform of  $\cos(k_l x)$  in the bounce motion of an electron in the potential well ( $dx/dt = -eE_{sc}(x)/m$ )

$$G_{l,n}(\varepsilon) = \frac{1}{T} \left[ \int_0^T \cos[k_l x(\tau)] \cos\left(\frac{\pi n \tau}{T}\right) d\tau \right]. \quad (23)$$

The coefficients  $G_{l,n}(\varepsilon)$  can be effectively computed using the Fast Fourier Transform (FFT) method.

The Maxwell (20) together with the equations for the electron currents (21) and (23) comprise the complete system for determining the profiles of the RF electric field.

#### D. Calculation of the Electrostatic Potential

The electrostatic potential is obtained using the quasi-neutrality condition

$$n_i(x) = n_e(x) = \int_{\varphi(x)}^{\infty} f_0(\varepsilon) \sqrt{\varepsilon - \varphi(x)} d\varepsilon \quad (24)$$

where  $n_e(x)$  is the electron density profile and  $n_i(x)$  is the ion density profile given by a set of fluid conservation equations for ion density and ion momentum [30], [40]

$$\frac{\partial n_i}{\partial t} + \frac{\partial(n_i u_i)}{\partial x} = R_{\text{ion}} \quad (25)$$

and

$$\frac{\partial(n_i u_i)}{\partial t} + \frac{\partial(n_i u_i u_i)}{\partial x} = -\frac{n_i}{M_{\text{ion}}} \frac{\partial \phi(x)}{\partial x} - \nu_{\text{ion}} n_i u_i \quad (26)$$

where  $R_{\text{ion}}$  is the ionization rate,  $\nu_{\text{ion}}$  is the ion-neutral collision frequency and  $n_i$ ,  $u_i$ ,  $M_{\text{ion}}$  are ion density, velocity, and mass, respectively.

Equation (24) is solved in the form of a differential equation [20]

$$\frac{d\varphi}{dx} = -T_e^{\text{scr}}(x) \frac{d \ln[n_i(x)]}{dx} \quad (27)$$

where  $T_e^{\text{scr}}(x)$  is the electron screening temperature

$$T_e^{\text{scr}}(x) = \left[ \frac{1}{2n(x)} \int_{\varphi(x)}^{\infty} f_0(\varepsilon) \frac{d\varepsilon}{\sqrt{\varepsilon - \varphi(x)}} \right]^{-1} \quad (28)$$

and the electrostatic ambipolar potential can be obtained by integration of (27).

#### IV. DISCUSSION

The above described self-consistent system of equations gives a working tool for efficient, fast simulations of 1-D inductively coupled magnetized plasmas.

The total power deposited into plasma per unit square of side surface  $P$  can be computed as [1]

$$P = \frac{1}{4} \text{Re}(E^{+*} j^+ + E^{-*} j^-). \quad (29)$$

Also, the total deposited power is related to the electron energy diffusion coefficient  $D_\varepsilon(\varepsilon)$  as [28]

$$P = -\sqrt{2m} \int_0^{\infty} D_\varepsilon(\varepsilon) \frac{df_0(\varepsilon)}{d\varepsilon} d\varepsilon. \quad (30)$$

The agreement of the total power computed from (29) and (30) can be used as a good consistency check for the above described formalism during the numerical simulations.

For the sake of further analysis, it is convenient to express the deposited power as a function of the plasma resistance, or the real part of the plasma impedance  $Z$ , that is defined as

$$Z = Z_- + Z_+ = \frac{2\pi}{c} \frac{E_-(0)}{B_-(0)} + \frac{2\pi}{c} \frac{E_+(0)}{B_+(0)} \quad (31)$$

where  $E_\pm(0)$  and  $B_\pm(0)$  are the electric and magnetic field at the current sheath for the right and left polarized waves. The power deposited into plasma is related to the plasma impedance as

$$P = -I^2 \text{Re}(Z) \quad (32)$$

where  $I$  is the effective amplitude of the sheath current [1].

The surface impedance also can be used to estimate the skin depth

$$\delta = \frac{E}{-dE/dx} \Big|_{x=0}. \quad (33)$$

Using (14), one obtains  $dE/dx = -2\pi i \omega I / c^2$  and the skin depth (33) becomes

$$\delta = \frac{c^2 Z}{4\pi i \omega}. \quad (34)$$

For a purely inductive impedance,  $\delta$  is a real number, but in the general case  $\delta$  is complex. Eq. (34) is accurate only for a purely exponential profile of the electric field  $\exp(-x/\delta)$ . If the electric field profile is more complex (e.g., two length scales), calculation of the entire profile of the RF electric field is necessary, see [32] for an example.

### A. Analysis With a Given Maxwellian EEDF

For uniform plasmas with Maxwellian EEDF our formalism for calculation of the RF electric field [(20), (21), (23)] simplifies considerably. In this case, the surface impedance of a 1-D, bounded, uniform plasma of length  $L$  inductively driven by two current sheets with an applied external static magnetic field reads [28], [33]

$$Z = \frac{Z^l + Z^r}{2} \quad (35)$$

where

$$Z^{l,r} = \frac{16\pi i\omega}{c^2 L} \sum_{s=0}^{\infty} \frac{1}{k_s^2 - \omega^2/c^2 - Z_M\left(\frac{\omega \pm \Omega_c + i\nu}{k_s V_T}\right) / k_s \delta_a^3}. \quad (36)$$

Here, we introduce the anomalous skin depth

$$\delta_a = \left(\frac{c^2 V_T}{\omega_{pe}^2 \omega}\right)^{1/3} \quad (37)$$

where  $\omega_{pe} = (4\pi e^2 n/m)^{1/2}$  is the electron plasma frequency and  $Z_M(\xi)$  is the “standard” plasma dielectric function

$$Z_M(\xi) = \pi^{-1/2} \int_{-\infty}^{\infty} dt \frac{\exp(-t^2)}{t - \xi}. \quad (38)$$

In the limit of a semi-infinite uniform plasma,  $L \rightarrow \infty$ , the summation turns into an integral with  $dk = 2\pi/L$ , and (36) yields

$$Z_{\infty}^{l,r} = \frac{8i\omega}{c^2} \int_0^{\infty} dk \frac{1}{k^2 - \omega^2/c^2 - Z_M\left(\frac{\omega \pm \Omega_c + i\nu}{k V_T}\right) / k \delta_a^3}. \quad (39)$$

The expression for the plasma surface resistance following from (36) is given by

$$\text{Re } Z^{l,r} = \frac{16\pi i\omega}{c^2 L} \sum_{s=0}^{\infty} \frac{\frac{\text{Im } Z_M(\zeta)}{k_s \delta_a^3}}{\left[k_s^2 - \frac{\omega^2}{c^2} - \frac{\text{Re } Z_M(\zeta)}{k_s \delta_a^3}\right]^2 + \left[\frac{\text{Im } Z_M(\zeta)}{k_s \delta_a^3}\right]^2}. \quad (40)$$

where  $\zeta = (\omega \pm \Omega_c + i\nu)/k_s V_T$ .

As it can easily be seen from the dispersion equation for the cold collisionless plasma [1]

$$\frac{c^2 k^2}{\omega^2} = 1 - \frac{\omega_{pe}^2/\omega^2}{1 \mp \Omega_c/\omega} \quad (41)$$

for  $\omega < \omega_{pe}$  (where,  $\omega_{pe}$  is the electron plasma frequency), application of external magnetic field gradually changes the

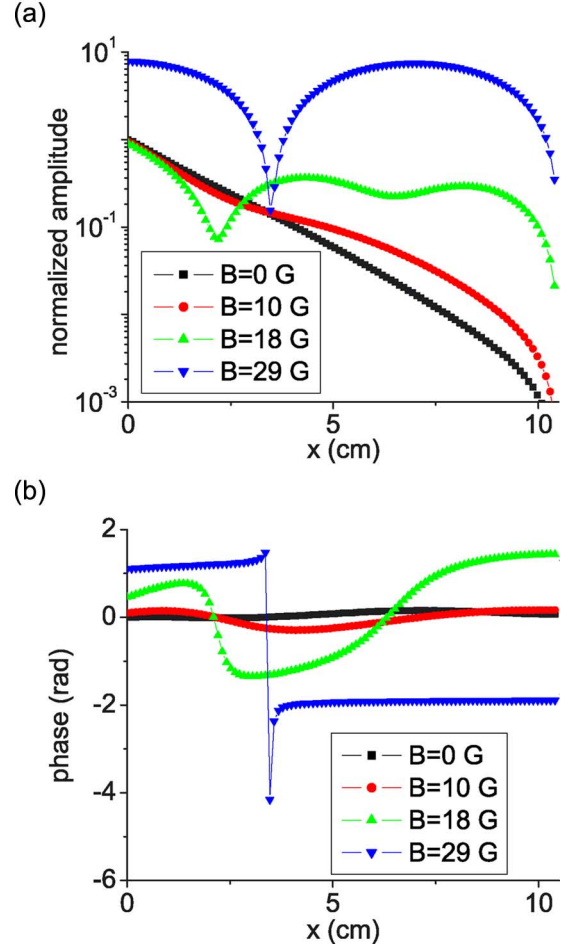


Fig. 14. Electric field profiles normalized by the electric field  $E(x=0, B=0)$ : (a) amplitude and (b) phase for different values of applied magnetic field for a uniform, bounded plasma. Plasma parameters are: half plasma length  $L/2 = 10.5$  cm, RF field frequency  $\omega/2\pi = 29$  MHz, electron temperature  $T_e = 4$  eV, electron collision frequency  $\nu = 1.2 \cdot 10^7$  s $^{-1}$ , and the plasma density  $n_e = 10^{11}$  cm $^{-3}$  [33]. (Color version available online at <http://ieeexplore.ieee.org>.)

plasma electrodynamics from the nonwave propagating regime (evanescent waves) for  $\Omega_c < \omega$ , to the regime of propagation of the right-hand circularly polarized wave  $\Omega_c > \omega$  (with the minus sign in the denominator of the (41) and with phase velocity less than the speed of light).

For the warm, collisional plasma, the main features of the above picture remain the same. The electric field profiles for different values of the applied magnetic field are plotted in Fig. 14. A transition is evident from the non-propagating ( $B < 10$  G) to the propagating ( $B > 10$  G) wave. Here, magnetic field

$$B_c = \frac{mc\omega}{e} \quad (42)$$

$B_c = 10$  G corresponds to ECR for a 29 MHz discharge. The electric field profile changes from almost exponential in the evanescent regime ( $B < 10$  G) to a wave pattern ( $B > 10$  G) [12], [33]. For  $B = 29$  G, a standing wave forms which corresponds to the Fourier-harmonic with the wave vector  $k_1 = 3\pi/L$ .

### B. Nonpropagating Regime and Electron–Cyclotron Resonance

In the warm plasma, the nonpropagating regime is described by anomalous skin effect for  $l_{\text{free}}/\delta_p > 1$ , or by the regular skin effect for  $l_{\text{free}}/\delta_p < 1$ , where  $l_{\text{free}} = V_T/\sqrt{\omega^2 + \nu^2}$  is the effective electron mean free path, and  $\delta_p$  is the RF field penetration depth. For  $\Omega_c < \omega$ , application of the external magnetic field leads to increased RF wave dumping and, consequently, to increased plasma resistance, due to gradual approach to the electron–cyclotron resonance. The electrons gyrating with the same frequency as the driving frequency  $\omega$  (with Dopplerr shift correction) feel the field of the right-polarized wave as almost constant and are effectively accelerated, resulting in enhanced heating, as it follows from the (40). For  $\omega \sim \Omega_c \gg \nu$ ,  $ReZ_M \sim 0$ , and  $ImZ_M$  is maximal which give the enhanced dumping if

$$k_s^2 > ImZ_M \left( \frac{\omega \pm \Omega_c + i\nu}{k_s V_T} \right) / k_s \delta_a^3. \quad (43)$$

The presense of the  $ImZ_M$  in the denominator of the (40), implying the self-consistent effect of dumping on the RF electric field, leads to Doppler shifting of the *electron-cyclotron resonance condition*

$$\omega \sim \Omega_c + k_s V_T. \quad (44)$$

At the exact condition of the electron–cyclotron resonance  $\Omega_c = \omega$ , the surface resistance of a collisionless plasma  $\nu \ll \omega$ , with plasma slab length much larger than the anomalous skin depth  $\delta_a$ , can be calculated from (39) (taking into account that at ECR  $ReZ_M(0) = 0$  and  $ImZ_M(0) = \sqrt{\pi}$ ). For the right-hand polarized wave

$$Z_{\text{ECR}}^r = \frac{8\pi^{5/6}}{3} \left( i + \frac{1}{\sqrt{3}} \right) \frac{\omega \delta_a}{c^2}. \quad (45)$$

Equation (45) predicts larger plasma surface resistance at the electron–cyclotron resonance with increasing RF field frequency  $\omega$  and RF field penetration depth. The latter can occur either due to increase of electron temperature or decrease of plasma density.

### C. Propagating Regime and Transmission Resonances

For the propagating regime increased plasma resistance, also, can take place, but due to a different mechanism—the possible transmission resonance [12], [33]. Increasing the external magnetic field above the ECR condition ( $B \geq 10$  G for 29 MHz) leads to further growth of the plasma surface resistance, as evident in Fig. 15. This is due to propagation of the right-hand polarized wave into the plasma. Analysis of the wave propagation is especially convenient in the cold plasma approximation. In the limit of high magnetic field, warm plasma effects are not important if

$$\Omega_c - \omega \gg V_T k_s \quad (46)$$

i.e., if the nonlocality length is small,  $V_T/(\Omega_c - \omega) \ll 1/k_s$ . Substituting the cold plasma limit of the dielectric function  $Z_M(\zeta) \rightarrow -\zeta^{-1}$  for  $\zeta \rightarrow \infty$  gives the poles of the electric field in (40)

$$\frac{c^2 k_p^2}{\omega^2} = 1 - \frac{\omega_{pe}^2/\omega^2}{1 \pm \Omega_c/\omega}. \quad (47)$$

For a typical magnetically enhanced ICP  $\omega$ ,  $\Omega_c \ll \omega_{pe}$ , and propagating modes exist only for the right-hand polarized wave with a wave vector

$$k_p = \frac{\omega_{pe}}{c\sqrt{\Omega_c/\omega - 1}}. \quad (48)$$

For a bounded plasma, transmission resonance occurs if an odd number of half-waves equals the plasma slab length, or  $k_p = k_s$ , which gives

$$\frac{(2s+1)\pi}{L} = \frac{\omega_{pe}}{c\sqrt{\Omega_c/\omega - 1}}. \quad (49)$$

Warm plasma effects can be neglected for not very high resonance numbers  $s$ , for which the nonlocality length is less than the wavelength  $V_T/(\Omega_c - \omega) \ll \pi L/(2s+1)$ .

Strong transmission resonances at the values of the magnetic field predicted by (49) are evident in Fig. 15. Note that the transmission resonances occur at different values of magnetic field for different plasma slab lengths. When (46) is satisfied, the surface resistance of cold plasma is the same as that of warm plasma. In the opposite case, transmission resonances are less pronounced due the wave dissipation through collisionless damping. The maximum value of the plasma surface resistance and the width of the transmission resonances are determined by a small dissipation, either due to collisional or collisionless damping described by  $Im(Z_M)$ . Note that a right-hand polarized wave reflects from a plasma–vacuum interface with a reflection coefficient  $R = 1 - 2\omega/ck_p$ . Since  $\omega/ck_p \ll 1$ ,  $R \simeq 1$  and the wave is trapped inside the plasma.

Let us now estimate the condition of existence of transmission resonances. Warm plasma effects can be neglected if  $k_p V_T \ll \Omega_c - \omega$ . Substituting  $k_p$  from (48) gives the minimum value of  $\Omega_c - \omega$  for a pronounced transmission resonance

$$\Omega_c - \omega \gg \left( \frac{V_T}{c} \omega_{pe} \omega^{1/2} \right)^{2/3}. \quad (50)$$

Substituting in turn  $\Omega_c - \omega$  from (50) into (48), gives the maximum value of the wave vector  $k_p$  for a pronounced transmission resonance

$$k_p \ll \frac{1}{\delta_a}. \quad (51)$$

That is, the wave length should be much longer than the anomalous skin effect length. This condition provides that the collisionless damping of the wave is small.

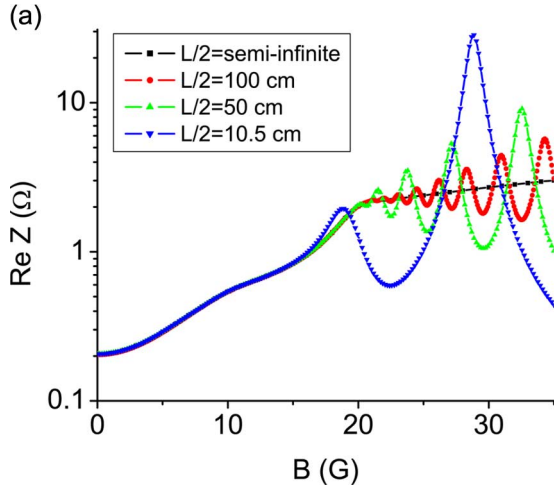


Fig. 15. Surface resistance of semi-infinite and bounded plasmas of different lengths as a function of the applied magnetic field for a uniform plasma with a Maxwellian EEDF. Discharge frequency is 29 MHz, the plasma density  $n_e = 10^{11} \text{ cm}^{-3}$  and the electron collision frequency  $\nu = 1.2 \cdot 10^7 \text{ s}^{-1}$ . (a) Warm plasma with the electron temperature  $T_e = 4 \text{ eV}$ . (b) Cold plasma with the electron temperature  $T_e \rightarrow 0$  (local approximation for electron current) [33]. (Color version available online at <http://ieeexplore.ieee.org>.)

In addition, (49) suggests that the minimum value of the plasma slab length to observe a pronounced transmission resonance should satisfy the relation

$$L \gg \pi \delta_a. \quad (52)$$

For short plasma lengths or low plasma densities, (52) is not satisfied and the transmission resonances are not observed. Fig. 16 shows the surface plasma resistance of warm bounded plasmas for different electron densities. When the electron density is less than  $n_e = 10^{10} \text{ cm}^{-3}$ , (52) is not satisfied and transmission resonances are not observed. As a result, the plasma surface resistance decreases with increasing applied magnetic field for magnetic fields larger than  $B_c$ . The disappearance of the transmission resonances for small lengths  $L = 10 \text{ cm}$  is shown at Fig. 17.

Strong transmission resonances may cause difficulty in coupling power to the plasma through a matching network, as was reported in [8] for magnetic fields  $B > 20 \text{ G}$ . These values of magnetic field appear to result in transmission resonances for the experimental plasma parameters in [8].

As evident in Fig. 15, increasing the length of a bounded plasma leads to a larger number of transmission resonance peaks. In the limit  $L \rightarrow \infty$ , these peaks overlap and the plasma surface resistance reaches an asymptotic curve. Substituting the cold plasma limit for the dielectric function  $Z_M(\zeta) \rightarrow -\zeta^{-1}$  as  $\zeta \rightarrow \infty$  and integrating (39) over the poles of the electric field,  $k = k_p$ , given by (48) yields the asymptotic value of the plasma surface resistance

$$Z_\infty^r = \frac{4\pi}{c\omega_{pe}} \sqrt{\omega(\Omega_c - \omega)}. \quad (53)$$

Also, it can be seen from Fig. 15 that for given magnetic field for  $\Omega_c > \omega$  the increase of the plasma length  $L$  leads to ap-

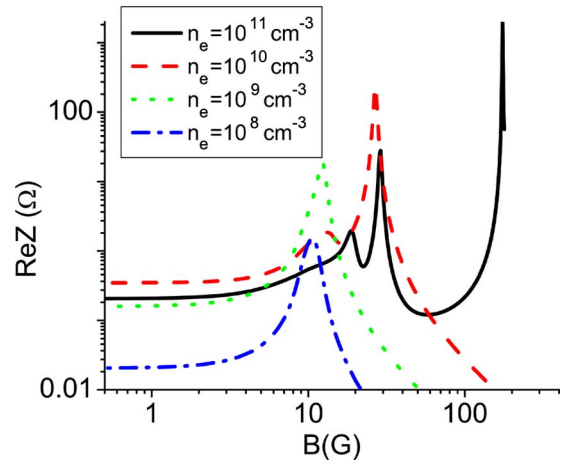


Fig. 16. Surface resistance of warm bounded uniform Maxwellian plasmas for different electron densities as a function of the applied magnetic field. Discharge parameters: RF field frequency  $\omega/2\pi = 29 \text{ MHz}$ , electron temperature  $T_e = 4 \text{ eV}$ , electron collision frequency  $\nu = 1.2 \cdot 10^7 \text{ s}^{-1}$ , and the plasma half-length  $L/2 = 10.5 \text{ cm}$  [33]. (Color version available online at <http://ieeexplore.ieee.org>.)

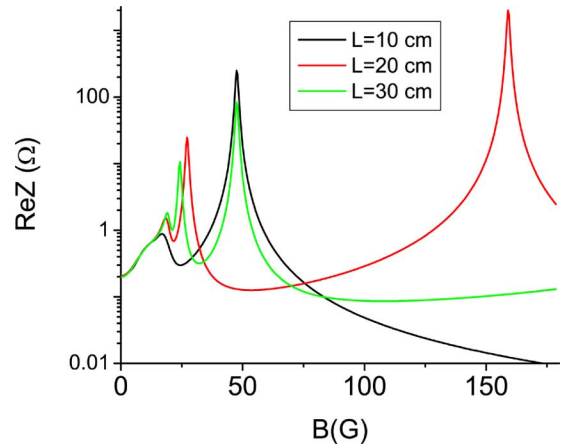


Fig. 17. Plasma resistance as a function of the applied magnetic field for different gap lengths and a given Maxwellian EEDF for the case of two current sheaths. Discharge parameters: the RF field frequency  $\omega/2\pi = 29 \text{ MHz}$ , the electron temperature  $T_e = 4 \text{ eV}$ , the electron density  $n_e = 10^{11} \text{ cm}^{-3}$ , and the gas pressure  $P_{\text{gas}} = 3 \text{ mtorr}$ . (Color version available online at <http://ieeexplore.ieee.org>.)

proaching by the surface resistance to its value for the semi-infinite plasma. This value, again, can be analytically described as the overlap of the multiple transmission resonances, broadened due to collisionless dumping or collisions (compare the cases of warm and cold plasmas in Fig. 15). The condition on plasma length for applicability of the limit of a semi-infinite plasma is that the width of resonance  $\delta k$  is larger than the distance between them  $dk$

$$\delta k > dk. \quad (54)$$

From (36), it follows that the distance between resonances is

$$dk = 2\pi/L. \quad (55)$$

Also, from (36), it follows that the width of a resonance is

$$\delta k = \frac{\text{Im}Z_M \left( \frac{\omega \pm \Omega_c + i\nu}{k_p V_T} \right)}{2k_p^2 \delta_a^3}. \quad (56)$$

Indeed, from (36) for the real part of surface impedance follows that the width of the resonance is given by

$$\left| k^2 - \omega^2/c^2 - \text{Re}Z_M \left( \frac{\omega \pm \Omega_c + i\nu}{k V_T} \right) / k \delta_a^3 \right| \leq \left| \text{Im}Z_M \left( \frac{\omega \pm \Omega_c + i\nu}{k V_T} \right) / k \delta_a^3 \right|. \quad (57)$$

Representing  $k = k_p + \delta k$ , where  $k_p$  is the root of the left hand of inequality in (58) and taking into account that  $k_p \gg \delta k$  and  $\text{Re}Z_M \gg \text{Im}Z_M$  (when condition in (51) is valid), (58) easily yields (56) for  $\delta k$ .

Substituting (56) for  $\delta k$  and (55) for  $dk$  into (54) gives

$$L > L_{\max} = \frac{4\pi k_p^2 \delta_a^3}{\text{Im}Z_M \left( \frac{\omega \pm \Omega_c + i\nu}{k_s V_T} \right)}. \quad (58)$$

This condition corresponds to strong dumping of the propagating wave on distance  $L_{\max}$ . It follows from the form of the dispersion equation for the propagating wave  $e^{-ikx}$  in unbounded plasma, which reads

$$k^2 - \omega^2/c^2 - Z_M \left( \frac{\omega \pm \Omega_c + i\nu}{k V_T} \right) / k \delta_a^3 = 0 \quad (59)$$

If wave dumping is weak, i.e.,  $\text{Im}Z_M \ll \text{Re}Z_M$ , than the imaginary part of the wave vector is small compared with the wave vector ( $\text{Im}k \ll \text{Re}k$ ), and  $\text{Re}k \simeq k_p$  from (48). The wave damping rate can then be easily obtained by equating the real and imaginary parts of (59), which for yields

$$\text{Im}k = \delta k \quad (60)$$

where  $\delta k$  is from (56).

#### D. Nonuniform Plasma

The electron–cyclotron and cavity resonance heating is, essentially, a wave–particle resonance type heating. It follows that the heating of the both types highly depends on the number of the resonant electrons, or electrons for which the resonant conditions are satisfied ( $|\omega - \Omega_c| \leq k_n v_T$  for ECR, and (41) with  $\Omega_c - \omega > k_n V_T$  for cavity resonance), but the actual form of the ambipolar electrostatic potential can greatly alter the number of present resonant electrons, that, in turn, can greatly affect the resonant heating.

In Fig. 18, the results of the numerical simulations of the dependence of the plasma resistance on applied  $B$  field are presented, for a given Maxwellian EEDF, uniform and nonuniform plasmas (*with* and *without* an ambipolar potential). The case of the one grounded electrode was considered. It is seen that the plasma resistivity is considerably enhanced at the electron–cyclotron resonant conditions ( $B_{\text{ext}} \approx 10$  G), which means the

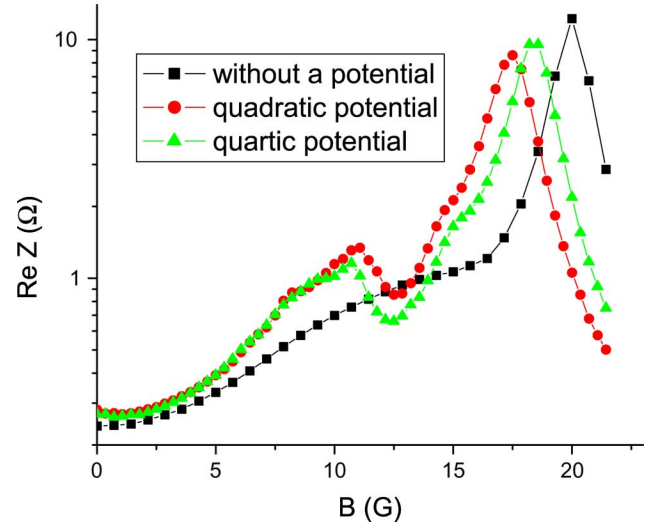


Fig. 18. Plasma resistance as a function of the applied magnetic field for uniform plasma (without an ambipolar potential) and for nonuniform plasmas (with  $\phi(x) = 4 \times (2x/L - 1)^2$  eV and  $\phi(x) = 4 \times (2x/L - 1)^4$  eV) for a given Maxwellian EEDF. Case of one grounded electrode. Discharge parameters: RF field frequency, discharge electron temperature, and the peak electron density are the same as in Fig. 1. Gas pressure  $P_{\text{gas}} = 3$  torr and the discharge gap is  $L = 10.5$  cm. (Color version available online at <http://ieeexplore.ieee.org>.)

larger number of the resonant electrons due to the presence of the ambipolar potential. The effect of enlargement of the number of resonant electrons in the nonuniform plasma at the bounce resonance condition was reported by authors in [6]. The main idea of it that the plasma electrons of different energies, bouncing in the ambipolar potential of a nonuniform plasma, have smaller spreading in a bounce frequency, comparing to the case of a uniform plasma. And if this frequency matches the resonant condition, it immediately gives a larger number of resonant electrons. For example, the plasma electrons of all energies bounce with the same frequency in the quadratic ambipolar potential. The condition of ECR for a bounded plasma, as it follows from the expression for the energy diffusion coefficient (13), is  $\omega = \Omega_b n + \Omega_c$ . It includes the bounce frequency and can be greatly affected by the ambipolar potential.

For the cavity resonance ( $B_{\text{ext}} \approx 20$  G) Fig. 18 reveals the lower plasma resistivity for nonuniform plasmas which can be attributed to the higher dumping in this case, caused by more resonant electrons (violations of the necessary condition [(46)]). It needs to be accentuated that non accounting for the electrostatic ambipolar potential (allowing electrons to bounce between walls that constrain plasma), as it is often done for simplicity, can results in erroneous description of plasma behavior at resonant conditions, due to aforementioned drastic influence of the electrostatic potential on the plasma heating.

#### V. RESULTS OF FULL SELF-CONSISTENT CALCULATIONS OF THE DISCHARGE PARAMETERS

To investigate the dependence of the parameters of a magnetized discharge on the magnitude of the applied magnetic  $B$  field, the full self-consistent simulations of the driving sheaths current (corresponding to coil current in two-dimensional (2-D) geometry), EEDF, RF electric field, plasma density, electron temperature, and ambipolar potential for a fixed deposited

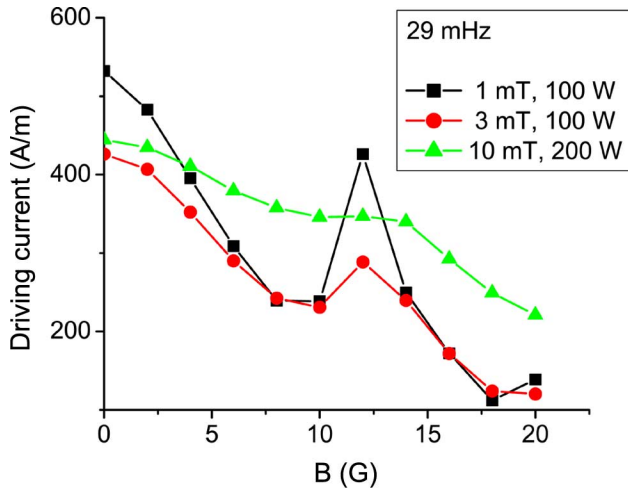


Fig. 19. Sheath current as a function of the applied magnetic field for full self-consistent discharge simulations for different deposited powers and gas pressures. The case of one grounded electrode. Discharge parameters: RF field frequency  $\omega/2\pi = 29$  MHz, the discharge gap  $L = 10.5$  cm, and the discharge cross section  $S_{\text{gross}} = 64\pi \text{ cm}^2$ . (Color version available online at <http://ieeexplore.ieee.org>.)

power have been performed for the case of one grounded electrode. Simulations described in this chapter were performed in order to compare the developed code with the data recently measured by Godyak *et al.* and given in [8]. All calculations have been done for 29 MHz driving frequency and for the values of the applied magnetic field from 0 to 20 G (for  $B > 20$  G the discharge is impossible to maintain due to macroscopic plasma instability [8]). The length and side area of the discharge was chosen 10.5 cm and  $64\pi \text{ cm}^2$  correspondingly.

Fig. 19 shows the dependence of the coil current on the  $B$  field for different given deposited power and pressures (correspond to different transport collision frequencies). As it seen in Fig. 19, the coil current has pronounced minima for  $B \sim 10$  G for low pressures  $P = 1, 3$  mtorr and the shallow minimum for  $P = 10$  mtorr. All these minima correspond to electron–cyclotron resonance, as it follows from (32) and the general behavior of the plasma resistance, given, for example, in Fig. 2. For constant deposited power, increase and the maxima of the plasma resistance correspond to decrease and minima of the coil current. The shallowness of the coil current minima for  $P = 10$  mtorr can be explained by collisional broadening. The same reasoning can be applied to the minima for  $B \sim 20$  G which corresponds to the cavity resonance. All of them are deeper than the corresponding ECR minima, because of larger plasma resistance at the cavity resonance (Fig. 2).

The profiles of the energy diffusion coefficient and the electron energy distribution function are given in Figs. 20 and 21, correspondingly. It is seen, that the largest electron energy diffusion coefficient in the region of low energy  $\varepsilon \leq 10$  eV is for  $B = 10$  G (corresponds to ECR). This results in more effective electron heating, leading to a larger plasma temperature, shown in Fig. 22. It suggests that at ECR condition the electrons interact with RF wave in the most efficient way (the damping rate is maximal), meanwhile at cavity resonance conditions plasma effectively gets transparent for some RF wave with small dumping of it by plasma electrons and the larger part of dissipated energy goes into the energy of the propagating wave.

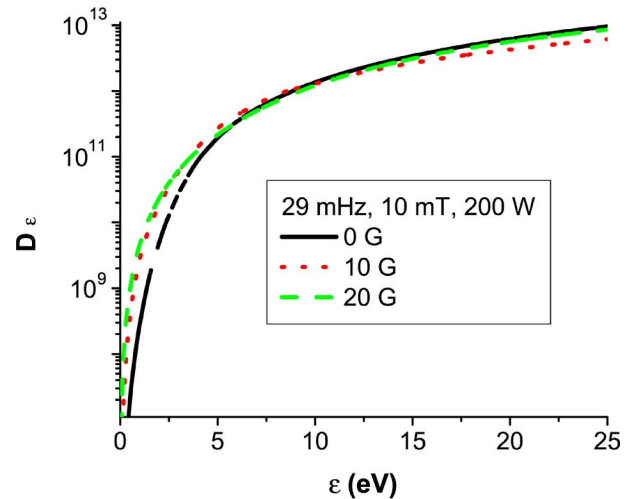


Fig. 20. Energy diffusion coefficient as a function of the electron energy for full self-consistent discharge simulations for different applied magnetic fields. Case of one grounded electrode. Discharge parameters are the same as in the Fig. 19. (Color version available online at <http://ieeexplore.ieee.org>.)

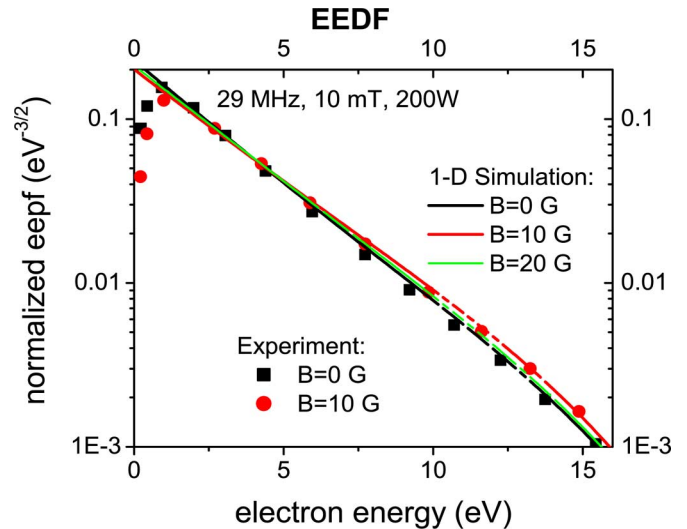


Fig. 21. Electron energy distribution function as a function of the electron energy for full self-consistent discharge simulations for different applied magnetic fields. Case of one grounded electrode. Discharge parameters are the same as in the Fig. 19. (Color version available online at <http://ieeexplore.ieee.org>.)

The steady-state electron energy distribution function is governed by following processes: the collisionless electron heating in the RF electric field, inelastic collisions with neutrals, and redistribution of energy among plasma electrons due to electron–electron collisions. We see in Fig. 21, that the EEDF shape is similar to the two-temperature EEDF [4], with the temperature of the tail of the distribution being lower than the temperature of the main body of the EEDF due to the onset of inelastic collisional losses. The EEDF corresponding to the electron–cyclotron resonance  $B = 10$  G is enriched by hot electrons due to the most effective heating and due to the largest rate of damping at the electron–cyclotron resonance.

The peak electron density (the density at the center of the discharge) as a function of the external magnetic field is plotted in Fig. 23 for different gas pressures and deposited powers. It is seen, that the minima of the electron density corresponds to the condition of electron–cyclotron resonance and, consequently,

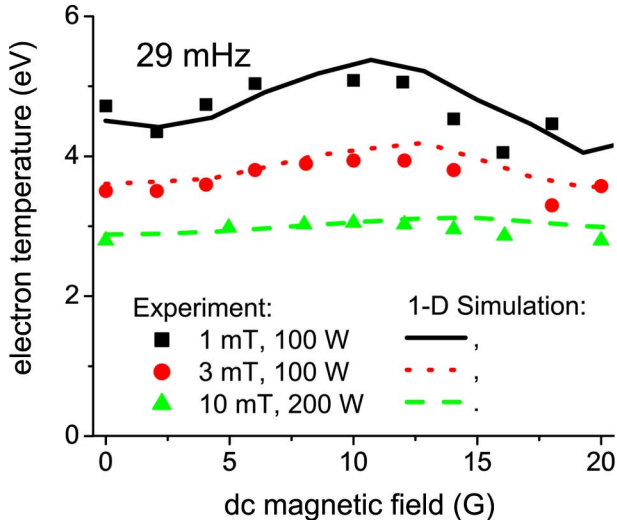


Fig. 22. Electron temperature at the discharge center as a function of the applied magnetic field for full self-consistent discharge simulations for different deposited powers and gas pressures. Case of one grounded electrode. Discharge parameters are the same as in Fig. 19. (Color version available online at <http://ieeexplore.ieee.org>.)

corresponds to maxima of the electron temperature (Fig. 22). For a constant deposited power, such a behavior of the plasma density as a function of electron temperature can be explained for 1-D geometry on the basis of the generalized power balance  $P_{\text{tot}} \sim n_e V_{\text{Bohm}}(T_e) \varepsilon_{\text{ion}}(T_e)$ , where  $V_{\text{Bohm}}(T_e)$  and  $\varepsilon_{\text{ion}}(T_e)$  are the Bohm velocity and the ionization price, respectively, and both of them are proportional to the electron temperature  $T_e$ . From this balance, it is obvious that the increase of the electron temperature for constant deposited power, inevitable, leads to the decrease of the peak electron plasma density.

The spatial profiles of the induced RF electric field for  $B = 0, 10, 20$  G that correspond to no magnetic field, ECR and cavity resonance, respectively, are plotted in Fig. 24. The main features of the wave propagation in the magnetized plasma, as decaying of the RF field due to skin effect for  $\omega > \Omega_c$  (evanescence) and the formation of the standing wave for  $\omega < \Omega_c$  (propagation) are explicitly shown. The wave length of the propagating wave for  $B = 20$  G is  $2\pi/k_3$  (corresponds to the harmonic mode with  $k_3 = 7\pi/2L$ ).

Figs. 21–24 depict the comparison of the calculated plasma temperature, density, and RF electric field profiles with the corresponding experimental values of them from [8]. It is clearly seen, that the simple 1-D ICP model of the present study, can describe with a reasonable accuracy the main properties of the real discharge. The apparent discrepancies, especially for the plasma density, can be attributed to the higher dimensionality of the actual discharge and are one of the our concerns for future work.

In conclusion, enhanced electron heating and larger plasma densities (for a given current in the coil) can be achieved if low-pressure ICP discharges are operated under the bounce resonance conditions. Self-consistent simulations of the discharge plasma surface resistance and the electron energy distribution function demonstrate the significance of explicit accounting for the nonuniform plasma density profile and the correct form of ambipolar electrostatic potential. Analysis of properties of a weakly magnetized inductively coupled discharges clearly reveals the phenomena of the electron–cyclotron and cavity reso-

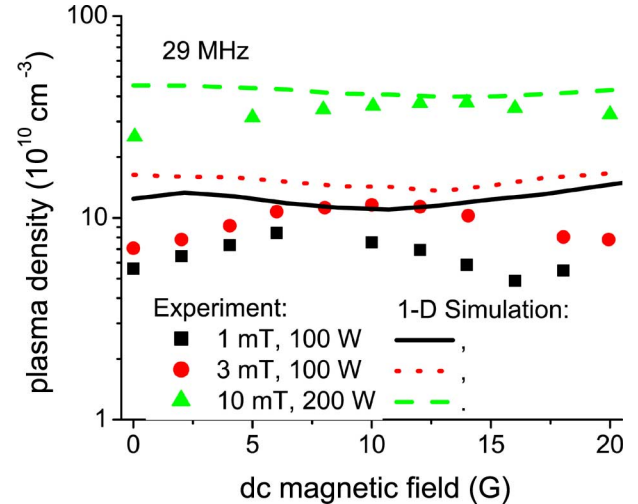


Fig. 23. Electron plasma density at the discharge center as a function of the applied magnetic field for full self-consistent discharge simulations for different deposited powers and gas pressures. Case of one grounded electrode. Discharge parameters are the same as in Fig. 19. (Color version available online at <http://ieeexplore.ieee.org>.)

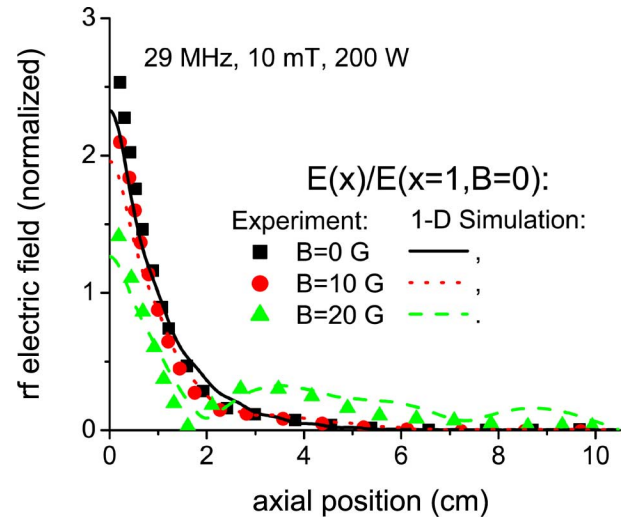


Fig. 24. Spatial profiles of the RF electric field along the sheath current as the functions of the discharge length for fully self-consistent discharge simulations for different applied magnetic fields. Case of one grounded electrode. Discharge parameters: RF field frequency  $\omega/2\pi = 29$  MHz, discharge gap  $L = 10.5$  cm, discharge cross-section  $S_{\text{gross}} = 64\pi$  cm<sup>2</sup>, gas pressure  $P_{\text{gas}} = 10$  mtorr, and deposited power  $P_{\text{tot}} = 200$  W. (Color version available online at <http://ieeexplore.ieee.org>.)

nances. Enhanced plasma heating at the electron–cyclotron resonance and the increase of deposited power with the increase of the applied magnetic field are demonstrated. The formalism developed in this work can be applied to many different problems for the description of wave–particle interaction in nonuniform plasmas.

#### APPENDIX A

If the effective mean free path

$$\lambda_{\text{eff}} = \frac{V_T}{\sqrt{(\omega - \Omega_c)^2 + \nu^2}} \quad (61)$$

is small compared with the discharge gap  $L$ , then two antennas act independently and the total deposited power into plasma

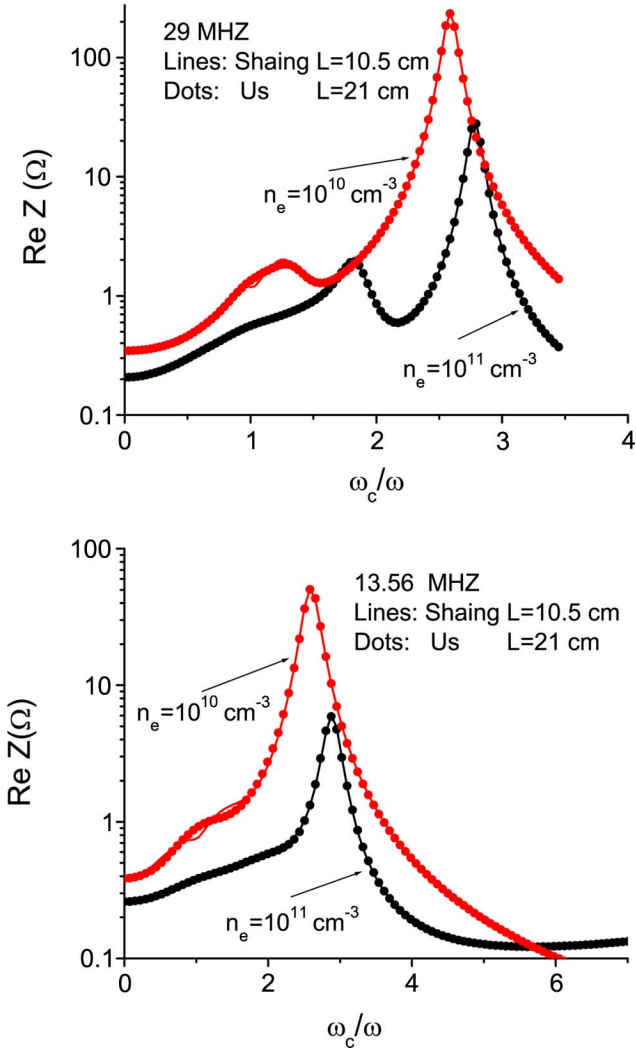


Fig. 25. Surface resistance as a function of a normalized electron-cyclotron frequency. Solid lines correspond to Shaing formalism for one grounded electrode with plasma length  $L$ . Dotted lines correspond to the case of two driving electrodes with plasma length  $2L$ . Shown: RF driving frequency (a) 29 MHz (b) 13.56 MHz. Electron temperature  $T_e = 4$  eV, electron collision frequency  $\nu = 1.2 \cdot 10^7$  s $^{-1}$ . (Color version available online at <http://ieeexplore.ieee.org>.)

can be viewed as sum of two halves, which are exactly the same as for one antenna at one plasma side and the grounded electrode ( $E = 0$ ) at another plasma side. Comparison between two solutions is shown in Fig. 25. In Fig. 25, the plasma surface resistance is calculated using Shaing's formalism [13] for one grounded electrode with plasma length  $L$ , and utilizing much simpler formalism of the two driving antennas with plasma length  $2L$  for typical plasma parameters. Apparently, agreement between two cases is very good, if not excellent.

For references purposes, the Shaing's formalism [13] for one grounded electrode for magnetized plasma of length  $L$  is given by

$$E^{l,r}(x) = \frac{4\pi i \omega I}{c^2 L} \sum_{s=0}^{\infty} \frac{\cos(k_s x)}{k_s^2 - \omega^2/c^2 - i\alpha K_s \left[ \frac{\nu \pm i\omega}{V_T} \right]} \quad (62)$$

$$K_s[a] = \int_0^{\infty} dy \frac{e^{-y^2}}{a^2 + (k_s y)^2} \left[ a + \frac{(-1)^s k_s y}{\sinh(aL/y)} \right] \quad (63)$$

where  $k_s = (2s + 1)\pi/(2L)$ ,  $\alpha = 2/(\pi\delta_a^3)$  and  $\delta_a^3 = V_T c^2 / \sqrt{\pi\omega\omega_{pe}^2}$ .

## APPENDIX B

The Boltzmann equation for the electron velocity distribution function reads

$$\begin{aligned} \frac{\partial f_1}{\partial t} + v_x \frac{\partial f_1}{\partial x} - \frac{eE_{SC}(x)}{m} \frac{\partial f_1}{\partial v_x} - \frac{eE_y(x,t)}{m} \frac{\partial (f_0 + f_1)}{\partial v_y} - \frac{eE_z(x,t)}{m} \frac{\partial (f_0 + f_1)}{\partial v_z} - \frac{eB_x(x,t)}{m} \left\{ v_z \frac{\partial f_1}{\partial v_y} - v_y \frac{\partial f_1}{\partial v_z} \right\} \\ = St(f_0 + f_1), \end{aligned} \quad (64)$$

where  $E_{SC}(x) = -d\phi(x)/dx$  is the stationary electric field due to the space charge,  $E_y(x,t)$  and  $E_z(x,t)$  are components of the nonstationary RF electric field, and  $St(f)$  is the collision integral. Note, the RF magnetic field drops out from (65) as  $\vec{v} \times \vec{B}_{RF} * \partial f_0(\varepsilon) / \partial \vec{v} \equiv 0$ . In writing of the (65), the fact of constancy of  $f_0(\varepsilon)$  along the electron trajectory have been used:

$$v_x \frac{\partial f_0(\varepsilon)}{\partial x} - \frac{eE_{sc}(x)}{m} \frac{\partial f_0(\varepsilon)}{\partial v_x} = v_x \frac{\partial f_0(\varepsilon)}{\partial x} \Big|_{\varepsilon_x} = 0. \quad (66)$$

After applying the formalism [22], [37] of the standard quasi-linear theory, (65) splits into two equations: a linear one for  $f_1$

$$\begin{aligned} \frac{\partial f_1}{\partial t} + v_x \frac{\partial f_1}{\partial x} - \frac{eE_{SC}(x)}{m} \frac{\partial f_1}{\partial v_x} - \frac{eE_y(x,t)}{m} \frac{\partial f_0}{\partial v_y} - \frac{eE_z(x,t)}{m} \\ \times \frac{\partial f_0}{\partial v_z} - \frac{eB_x(x,t)}{m} \left\{ v_z \frac{\partial f_1}{\partial v_y} - v_y \frac{\partial f_1}{\partial v_z} \right\} = St(f_1) \end{aligned} \quad (67)$$

and a quasi-linear one for  $f_0$

$$-\frac{eE_y(x,t)}{m} \frac{df_1}{dv_y} + \frac{eE_z(x,t)}{m} \frac{df_1}{dv_z} = \overline{St(f_0)}. \quad (68)$$

Here, the bar denotes space-time averaging over the phase space available to electrons with total energy  $\varepsilon$  [29], [34], [39].

Representing the RF electric field  $E_y(x,t) = E_{y0}(x) \exp(-i\omega t)$  and the anisotropic part of the EVDF  $f_1 = f_{10} \exp(-i\omega t)$ , as harmonic functions (where  $\omega$  is the discharge frequency), using the Bhatnagar-Gross-Krook (BGK) approximation,  $St(f_1) = -\nu f_1$  [28], and omitting the subscript 0 in the amplitudes, (68) can be rewritten as

$$\begin{aligned} -i\omega f_1 + v_x \frac{\partial f_1}{\partial x} \Big|_{\varepsilon_x} - \frac{ev_{\perp}}{2} (E^+ e^{-i\phi} + E^- e^{i\phi}) \frac{df_0}{d\varepsilon} \\ + \Omega_c \frac{df_1}{d\phi} = -\nu f_1 \end{aligned} \quad (69)$$

where  $\nu$  is the transport collision frequency,  $\varepsilon_x = mv_x^2/2 + \varphi(x)$  is the total energy along the  $x$  axis and  $\varphi(x) = -e\phi(x)$  is the electron potential energy. The left-hand and right-hand polarized RF fields,  $E^+$ , and  $E^-$ , are defined by the relations:  $E^+ = E_y + iE_z$  and  $E^- = E_y - iE_z$ . The electron cyclotron frequency

is defined as  $\Omega_c = eB_x/m$  and the gyrophase angle  $\phi$  is such that  $v_y = v_\perp \cos\phi$  and  $v_z = v_\perp \sin\phi$ .

After Fourier expansion of (70) with respect to the gyrophase angle  $\phi$

$$f_1 = \sum_q f_1^q e^{iq\phi} = f_1^+ e^{i\phi} + f_1^- e^{-i\phi} + \text{other}. \quad (70)$$

one can get the equations for  $q = \pm 1$

$$-i\omega f_1^+ + v_x \frac{\partial f_1^+}{\partial x} \Big|_{\varepsilon_x} - \frac{ev_\perp}{2} E^- \frac{df_0}{d\varepsilon} + i\Omega_c f_1^+ = -\nu f_1^+. \quad (71)$$

and

$$-i\omega f_1^- + v_x \frac{\partial f_1^-}{\partial x} \Big|_{\varepsilon_x} - \frac{ev_\perp}{2} E^+ \frac{df_0}{d\varepsilon} - i\Omega_c f_1^- = -\nu f_1^-. \quad (72)$$

Equations (71) and (72) can be effectively solved by transformation to the variable angle of the bounce motion

$$\theta(x, \varepsilon_x) = \frac{\pi \text{sgn}(v_x)}{T(\varepsilon_x)} \int_{x_-}^x \frac{dx}{|v_x(\varepsilon_x)|} \quad (73)$$

where  $T$  is half of the bounce period of the electron motion in the potential well  $\varphi(x)$

$$T(\varepsilon_x) = \int_{x_-}^{x_+} \frac{dx}{|v_x(\varepsilon_x)|}. \quad (74)$$

Making use of the Fourier series

$$g(x, \varepsilon_x) = \sum_{n=-\infty}^{\infty} g_n \exp(in\theta) \quad (75)$$

$$g_n = \frac{1}{2\pi} \left[ \int_{-\pi}^{\pi} g(\theta, \varepsilon_x) \exp(-in\pi\theta) d\theta \right] \quad (76)$$

Equations (71) and (72) simplify to

$$(in\Omega_b - i\omega + i\Omega_c + \nu) f_{1n}^+ = eE_n^- \frac{v_\perp}{2} \frac{df_0}{d\varepsilon} \quad (77)$$

and

$$(in\Omega_b - i\omega - i\Omega_c + \nu) f_{1n}^- = eE_n^+ \frac{v_\perp}{2} \frac{df_0}{d\varepsilon} \quad (78)$$

where  $\Omega_b(\varepsilon_x) = \pi/T(\varepsilon_x)$  is the electron bounce frequency in the potential well, and

$$E_n^\pm(\varepsilon_x) = \frac{1}{\pi} \left[ \int_0^\pi E^\pm(\theta) \cos(n\theta) d\theta \right]. \quad (79)$$

Solving the above equations we arrive to the expressions for the symmetrical part of  $f_1^\pm$  as follows:

$$\begin{aligned} f_{1s}^\pm(x, \varepsilon_x) &\equiv \frac{1}{2} (f_1^\pm(v_x > 0) + f_1^\pm(v_x < 0)) \\ &= -m \frac{v_\perp}{2} V_\perp^\pm(x, \varepsilon_x) \frac{df_0}{d\varepsilon} \end{aligned} \quad (80)$$

where

$$V_\perp^\pm(x, \varepsilon_x) = -\frac{e}{m} \sum_{n=-\infty}^{\infty} \frac{E_n^\mp \cos[n\theta(x)]}{in\Omega_b - i(\omega \mp \Omega_c) + \nu}. \quad (81)$$

Knowing the symmetrical part of the anisotropic contribution to the EVDF  $f_{1s} = f_{1s}^+ e^{i\phi} + f_{1s}^- e^{-i\phi}$ , one can average (68) according to

$$\overline{\text{Term}(x, \mathbf{v})}(\varepsilon) = \int_{x_-}^{x_+} dx v(x, \varepsilon) \text{Term}[x, v(x, \varepsilon)], \quad (82)$$

$$v(x, \varepsilon) = \sqrt{2[\varepsilon - \varphi(x)]/m}. \quad (83)$$

and obtain the final (8) for the main part  $f_0$ .

## REFERENCES

- [1] M. A. Lieberman and A. J. Lichtenberg, *Principles of Plasma Discharges and Materials Processing*. New York: Wiley, 1994.
- [2] F. F. Chen and J. P. Chang, *Lecture notes on Principles of Plasma Processing*. New York: Kluwer/Plenum, 2003.
- [3] V. A. Godyak, "Plasma phenomena in inductive discharges," *Plasma Phys. Control. Fusion*, vol. 45, p. A399, 2003.
- [4] M. A. Lieberman and V. A. Godyak, "From Fermi acceleration to collisionless discharge heating," *IEEE Trans. Plasma Sci.*, vol. 26, pp. 955-986, Jun. 1998.
- [5] V. I. Kolobov and D. J. Economou, "The anomalous skin effect in gas discharge plasmas," *Plasma Sources Sci. Technol.*, vol. 6, p. 1, 1997.
- [6] O. V. Polomarov, C. E. Theodosiou, and I. D. Kaganovich, "Enhanced collisionless heating in a nonuniform plasma at the bounce resonance condition," *Phys. Plasmas*, vol. 12, p. 080704, 2005.
- [7] I. D. Kaganovich, O. V. Polomarov, and C. E. Theodosiou, "Landau damping and anomalous skin effect in low-pressure gas discharges: Self-consistent treatment of collisionless heating," *Phys. Plasmas*, vol. 11, no. 5, p. 2399, 2004.
- [8] V. A. Godyak and B. M. Alexandrovich, "Plasma and electrical characteristics of inductive discharge in a magnetic field," *Phys. Plasmas*, vol. 11, p. 3553, 2004.
- [9] P. M. Platzman and S. J. Buchsbaum, "Wave Propagation along a Magnetic Field in a Warm Plasma," *Phys. Rev.*, vol. 123, p. 1004, 1962.
- [10] G. A. Baraff, "Transmission of Electromagnetic Waves through a Conducting Slab. II. The Peak at Cyclotron Resonance," *Phys. Rev.*, vol. 167, p. 625, 1968.
- [11] H.-J. Lee, I.-D. Yang, and K.-W. Whang, "The effects of magnetic fields on a planar inductively coupled argon plasma," *Plasma Sources Sci. Technol.*, vol. 5, p. 383, 1996.
- [12] S. S. Kim, C. S. Chang, N. S. Yoon, and K. W. Whang, "Inductively coupled plasma heating in a weakly magnetized plasma," *Phys. Plasmas*, vol. 6, p. 2926, 1999.
- [13] K. C. Shaing and A. Y. Aydemir, "Collisionless electron heating in inductively coupled discharges," *Phys. Plasmas*, vol. 4, p. 3163, 1997.
- [14] C. W. Chung, K.-I. You, S. H. Seo, S. S. Kim, and H. Y. Chang, "The electron bounce resonance in a low-pressure solenoidal inductive discharge," *Phys. Plasmas*, vol. 8, p. 2992, 2001.
- [15] C. W. Chung, S. S. Kim, S. H. Seo, and H. Y. Chang, "The finite size effect in a planar inductively coupled plasma," *J. Appl. Phys.*, vol. 88, p. 1181, 2000.

[16] V. A. Godyak and V. I. Kolobov, "Negative Power Absorption in Inductively Coupled Plasma," *Phys. Rev. Lett.*, vol. 79, p. 4589, 1997.

[17] ———, "Effect of Collisionless Heating on Electron Energy Distribution in an Inductively Coupled Plasma," *Phys. Rev. Lett.*, vol. 81, p. 369, 1998.

[18] Y. O. Tyshetskiy, A. I. Smolyakov, and V. A. Godyak, "Reduction of Electron Heating in the Low-Frequency Anomalous-Skin-Effect Regime," *Phys. Rev. Lett.*, vol. 90, p. 255002, 2003.

[19] G. Mumken, "Spatial profiles of a planar inductively coupled discharge in argon," *J. Phys. D, Appl. Phys.*, vol. 32, p. 804, 1999.

[20] S. V. Berezhnoi, I. D. Kaganovich, and L. D. Tsengin, "Fast modeling of low pressure radio-frequency collisional capacitively coupled discharge and investigation of nonMaxwellian electron distribution function," *Plasma Sources Sci. Technol.*, vol. 7, p. 268, 1998.

[21] I. D. Kaganovich, V. I. Kolobov, and L. D. Tsengin, "Stochastic electron heating in bounded radio-frequency plasmas," *Appl. Phys. Lett.*, vol. 69, p. 3818, 1996.

[22] Y. M. Aliev, I. D. Kaganovich, and H. Schluter, "Collisionless electron heating in RF gas discharges. I. Quasilinear theory," *Phys. Plasmas*, vol. 4, p. 2413, 1997.

[23] U. Buddemeier and I. Kaganovich, "Collisionless electron heating in RF gas discharges. II. Role of collisions and nonlinear effects," in *Electron Kinetics and Applications of Glow Discharges*, ser. NATO ASI Series B, U. Korsthagen and L. Tsengin, Eds. New York: Plenum, 1998, vol. 367, Physics.

[24] I. D. Kaganovich, "Effects of Collisions and Particle Trapping on Collisionless Heating," *Phys. Rev. Lett.*, vol. 82, p. 327, 1999.

[25] M. Koepke, R. F. Ellis, R. P. Majeski, and M. J. McCarick, "Experimental Observation of Bounce-Resonance Landau Damping in an Axisymmetric Mirror Plasma," *Phys. Rev. Lett.*, vol. 56, p. 1256, 1986.

[26] B. P. Cluggish, J. R. Danielson, and C. F. Driscoll, "Resonant Particle Heating of an Electron Plasma by Oscillating Sheaths," *Phys. Rev. Lett.*, vol. 81, p. 353, 1998.

[27] B. E. Meierovich, "Anomalous skin effect in a cylindrical conductor located in a magnetic field," *Sov. Phys. JETP*, vol. 31, p. 149, 1971.

[28] I. D. Kaganovich and O. V. Polomarov, "Self-consistent system of equations for a kinetic description of the low-pressure discharges accounting for the nonlocal and collisionless electron dynamics," *Phys. Rev. E*, vol. 68, p. 026411, 2003.

[29] I. D. Kaganovich and L. D. Tsengin, "The space-time-averaging procedure and modeling of the RF discharge II. Model of collisional low-pressure RF discharge," *IEEE Trans. Plasma Sci.*, vol. 20, no. 2, p. 66, Apr. 1992.

[30] B. Ramamurthi, D. J. Economou, and I. D. Kaganovich, "Effects of nonlocal conductivity on power absorption and plasma density profiles for low pressure inductively coupled discharges," *Plasma Sources Sci. Technol.*, vol. 11, p. 170, 2002.

[31] M. M. Turner, "Collisionless electron heating in an inductively coupled discharge," *Phys. Rev. Lett.*, vol. 71, p. 1844, 1993.

[32] I. D. Kaganovich, O. V. Polomarov, and C. E. Theodosiou, "Revisiting the anomalous RF field penetration into a warm plasma," *IEEE Trans. Plasma Sci.*, vol. 34, no. 3, pp. 696–717, Jun. 2006.

[33] O. V. Polomarov, C. E. Theodosiou, and I. D. Kaganovich, "Effectiveness of electron-cyclotron and transmission resonance heating in inductively coupled plasmas," *Phys. Plasmas*, vol. 12, p. 104505, 2005.

[34] L. D. Tsengin and Y. B. Golubovskii, "Positive column of a low-density, low-pressure discharge. I. Electron energy distribution," *Sov. Phys. Tech. Phys.*, vol. 22, p. 1066, 1977.

[35] V. L. Ginzburg and A. V. Gurevich, "Nonlinear phenomena in a plasma located in an alternating electromagnetic field," *Sov. Phys. Usp.*, vol. 3, p. 115, 1960.

[36] I. D. Kaganovich, M. Misina, R. Gijbels, and S. V. Berezhnoi, "Electron Boltzmann kinetic equation averaged over fast electron bouncing and pitch-angle scattering for fast modeling of electron cyclotron resonance discharge," *Phys. Rev. E*, vol. 61, p. 1875, 2000.

[37] Y. M. Aliev, I. D. Kaganovich, and H. Schluter, "Collisionless Electron Heating in RF Gas Discharges. I. Quasilinear Theory," in *Electron Kinetics and Applications of Glow Discharges*, ser. NATO ASI Series B, U. Korsthagen and L. Tsengin, Eds. New York: Plenum, 1998, vol. 367, Physics.

[38] B. E. Meierovich, "The anomalous skin-effect in thin cylindrical conductors," *Sov. Phys. JETP*, vol. 30, p. 782, 1970.

[39] I. D. Kaganovich and L. D. Tsengin, "Low-pressure RF discharge in the free-flight regime," *IEEE Trans. Plasma Sci.*, vol. 20, no. 2, pp. 86–92, Apr. 1992.

[40] B. Ramamurthi, D. J. Economou, and I. D. Kaganovich, "Effect of electron energy distribution function on power deposition and plasma density in an inductively coupled discharge at very low pressures," *Plasma Sources Sci. Technol.*, vol. 12, p. 302, 2002.



**Oleg V. Polomarov** received the diploma and the M.S. degree in theoretical physics from the Kiev State University, Kiev, Ukraine, in 1992 and the Ph.D. degree in plasma physics from the University of Toledo, Toledo, OH, in 2005.

Presently, he is a Postdoctoral Fellow at the Institute for Fusion Studies, the University of Texas at Austin, Austin. His primary research interests are kinetic aspects of discharge modeling, nonlinear dynamics and resonant excitation of strong plasma waves.



**Constantine E. Theodosiou** received the diploma from the University of Athens, Athens, Greece, in 1977 and the M.S. and Ph.D. degrees from the University of Chicago, Chicago, IL, all in physics.

Following a two-year postdoctoral at Johns Hopkins University, Baltimore, MD, he spent two years at the University of Freiburg, Freiburg, Germany, as an Alexander von Humboldt Fellow. After a year as a Visiting Faculty Member at Drexel University, Philadelphia, PA, he joined in 1981 the Physics and Astronomy Department at the University of Toledo,

Toledo, OH, where he is currently Professor of Physics and Associate Dean for the Natural Sciences and Mathematics. His primary research interests include calculations of atomic structure, atomic collisions, photon-atom interactions, and computer simulations of gas discharges, e.g., in plasma display panels.



**Igor D. Kaganovich** received the Ph.D. degree from Ioffe Physical Technical Institute, St. Petersburg, Russia.

He is a Research Physicist at Princeton Plasma Physics Laboratory (PPPL). His research is on plasma physics for controlled fusion, with focus on heavy ion fusion, and plasma applications, in particular, gas discharge modeling. Three books have referenced his results.

Dr. Kaganovich was the recipient of the Alexander von Humboldt Fellowship in 1996.



**Demetre J. Economou** received the Ph.D. degree in chemical engineering from the University of Illinois, Urbana-Champaign, in 1986.

Since that time, he has been with the Chemical Engineering Department, the University of Houston, Houston, TX, where currently he is a John and Rebecca Moores Professor and the Associate Chairman of the Department. His research interests include plasma science and technology and nanotechnology with applications principally in electronic materials processing. He is the author or coauthor of over 140

papers and book chapters in these areas.



**Badri N. Ramamurthi** received the B.Tech. degree in chemical engineering from the Indian Institute of Technology, Chennai, India, in 1996 and the Ph.D. degree in chemical engineering from the University of Houston, Houston, TX, in 2002. His Ph.D. research consisted of the investigation of nonlocal electron heating mechanisms in low-pressure ICP plasma discharges.

Since 2002, he has been at the General Electric Global Research Center and is currently a Research Scientist in the area of sustainable energy, wherein,

he has developed physics-based models to understand the behavior of fuel cells.